

## FIRST SPECTROSCOPIC EVIDENCE FOR HIGH IONIZATION STATE AND LOW OXYGEN ABUNDANCE IN LY $\alpha$ EMITTERS <sup>† ‡</sup>

KIMIHIKO NAKAJIMA <sup>1,3</sup>, MASAMI OUCHI <sup>2,3</sup>, KAZUHIRO SHIMASAKU <sup>1,4</sup>, TAKUYA HASHIMOTO <sup>1</sup>, YOSHIAKI ONO <sup>1,2</sup>,  
AND JANICE C. LEE <sup>5,6,7,8</sup>

*Submitted to ApJ*

### ABSTRACT

We present results from Keck/NIRSPEC and Magellan/MMIRS follow-up spectroscopy of Ly $\alpha$  emitters (LAEs) at  $z = 2.2$  identified in our Subaru narrowband survey. We successfully detect H $\alpha$  emission from seven LAEs, and perform a detailed analysis of six LAEs free from AGN activity, two out of which, CDFS-3865 and COSMOS-30679, have [O II] and [O III] line detections. They are the first [O II]-detected LAEs at high- $z$ , and their [O III]/[O II] ratios and  $R23$ -indices provide the first simultaneous determinations of ionization parameter and oxygen abundance for LAEs. CDFS-3865 has a very high ionization parameter ( $q_{ion} = 2.4_{-0.9}^{+2.0} \times 10^8 \text{ cm s}^{-1}$ ) and a low oxygen abundance ( $12 + \log(\text{O}/\text{H}) = 7.84_{-0.25}^{+0.24}$ ) in contrast with moderate values of other high- $z$  galaxies such as Lyman-break galaxies (LBGs). COSMOS-30679 also possesses a relatively high ionization parameter ( $q_{ion} = (3.4\text{--}15) \times 10^7 \text{ cm s}^{-1}$ ) and a low oxygen abundance ( $12 + \log(\text{O}/\text{H}) = 8.08\text{--}8.67$ ), and falls below the mass-metallicity relation of  $z \sim 2$  LBGs. Similarly, a low metallicity of  $12 + \log(\text{O}/\text{H}) < 8.4$  is independently indicated for typical LAEs from a composite spectrum and the [N II]/H $\alpha$  index. Such high ionization parameters and low oxygen abundances can be found in local star-forming galaxies, but this extreme local population occupies only  $\lesssim 0.3\%$  of the SDSS spectroscopic galaxy sample with a number density  $\gtrsim 10$  times smaller than that of LAEs. With their high ionization parameters and low oxygen abundances, LAEs would represent an early stage of galaxy formation dominated by massive stars in compact star-forming regions. Thus, low-mass galaxies such as LAEs produce ionizing photons efficiently probably with a high escape fraction achieved by density-bounded HII regions, which would significantly contribute to cosmic reionization at  $z > 6$ . More than half of our LAEs have a larger EW(Ly $\alpha$ ) than expected from an instantaneous burst model at a given EW(H $\alpha$ ), suggesting that the majority of LAEs rather experience a more extended and continuous star-formation history.

*Subject headings:* galaxies: evolution

### 1. INTRODUCTION

Ly $\alpha$  emitters (LAEs), galaxies commonly observed at high redshifts with strong Ly $\alpha$  emission, are considered to be low-mass, young galaxies as suggested from their small sizes, faint continua, and low masses inferred from spectral energy distribution (SED) fitting (e.g.,

Venemans et al. 2005; Gawiser et al. 2006; Pirzkal et al. 2007; Overzier et al. 2008). LAEs are therefore likely to represent galaxies in the early stages of galaxy evolution. More directly, Cowie et al. (2011) investigate rest-frame optical nebular lines of LAEs at low redshifts ( $z \sim 0.3$ ). The authors find that a large portion of LAEs (75%) have equivalent width (EW) of H $\alpha$   $> 100 \text{ \AA}$ , and that LAEs on average have lower metallicities and younger ages than the UV-continuum sample. These findings are consistent with the idea that LAEs are galaxies in early stages of galaxy formation. At higher redshifts, LAEs are efficiently detected thanks to narrowband imaging techniques which have enriched our knowledge about the younger universe (e.g., Cowie & Hu 1998; Malhotra & Rhoads 2002; Ouchi et al. 2003; Gawiser et al. 2006; Shimasaku et al. 2006; Gawiser et al. 2007; Gronwall et al. 2007; Ouchi et al. 2008; Nilsson et al. 2009; Guaita et al. 2010; Finkelstein et al. 2011; Nakajima et al. 2012). However, more direct evidence supporting the idea that high redshift LAEs are in an early evolutionary phase of formation is still needed.

The gas-phase metallicity is a key property of galaxies, since it is a record of their star-formation histories. This physical quantity is relatively easily constrained with line ratios of nebular lines at rest-frame optical wavelengths (e.g., Nagao et al. 2006). Another key quantity is the ionization parameter, defined as the ratio of the mean

nakajima@astron.s.u-tokyo.ac.jp

<sup>1</sup> Department of Astronomy, Graduate School of Science, The University of Tokyo, 7-3-1 Hongo, Bunkyo-ku, Tokyo 113-0033, Japan

<sup>2</sup> Institute for Cosmic Ray Research, The University of Tokyo, 5-1-5 Kashiwanoha, Kashiwa, Chiba 277-8582, Japan

<sup>3</sup> Kavli Institute for the Physics and Mathematics of the Universe (WPI), The University of Tokyo, 5-1-5 Kashiwanoha, Kashiwa, Chiba 277-8583, Japan

<sup>4</sup> Research Center for the Early Universe, Graduate School of Science, The University of Tokyo, Tokyo 113-0033, Japan

<sup>5</sup> Space Telescope Science Institute, Baltimore, MD, USA

<sup>6</sup> Visiting Astronomer, SSC/IPAC, Caltech, Pasadena, CA, USA

<sup>7</sup> Observatories of the Carnegie Institution of Washington, 813 Santa Barbara Street, Pasadena, CA 91101, USA

<sup>8</sup> Carnegie Fellow

<sup>†</sup> Some of the data presented herein were obtained at the W.M. Keck Observatory, which is operated as a scientific partnership among the California Institute of Technology, the University of California and the National Aeronautics and Space Administration. The Observatory was made possible by the generous financial support of the W.M. Keck Foundation.

<sup>‡</sup> Based in part on data collected at Subaru Telescope, which is operated by the National Astronomical Observatory of Japan.

ionizing photon flux to the mean hydrogen atom density. Since the excitation of the HII region is sensitive to the age distribution of the exciting stars, the ionization parameter provides a rough estimate of age of a galaxy (e.g., Dopita et al. 2006). A large ionization parameter is observed from a galaxy dominated with massive stars, which is a sign that the galaxy is in an early stage of galaxy formation. Determining the ionization parameter requires two emission lines of different ionization stages of a same element, such as [O II] and [O III] (e.g., Kewley & Dopita 2002).

However, well-defined samples of LAEs are generally located at very high redshifts ( $3 < z < 7$ ), where rest-frame optical nebular lines are redshifted into infrared wavelengths. Recently, Finkelstein et al. (2011) and Nakajima et al. (2012) instead take advantage of LAEs at moderately high redshifts ( $z \sim 2$ ), where the nebular lines up to H $\alpha$  are observable from the ground in the near-infrared (NIR) windows.

These studies extend the metallicity censuses to galaxies with strong Ly $\alpha$  emission. Finkelstein et al. (2011) obtain NIR spectra for two  $z \sim 2.4$  LAEs, and find that at least one LAE appears to be less chemically enriched than  $z \sim 2$  continuum-selected galaxies at similar stellar masses (Erb et al. 2006a). Nakajima et al. (2012) estimate average line fluxes for [O II] $\lambda$ 3727 and H $\alpha$ + [N II] $\lambda$ 6584 for  $z = 2.2$  LAEs by stacking 1.18 and 2.09  $\mu$ m narrowband images for more than 100 LAEs, and place a firm lower-limit for the average metallicity of this population. Interestingly, the lower-limit is higher than expected for its stellar mass at the redshift.

In contrast to the gas-phase metallicities, the ionization parameters of LAEs are unknown. Such measurements have only been obtained for bright galaxies such as Lyman-break galaxies (LBGs) or strongly lensed galaxies at high- $z$  (e.g., Pettini et al. 2001; Hainline et al. 2009; Richard et al. 2011). Although the current number of measurements is small, ionization parameters of such high- $z$  galaxies are likely to be higher on average than those of local galaxies. A comparison of ionization parameters for LBGs and LAEs will enable us to discuss whether or not LAEs are young galaxies at high redshifts.

In order to obtain reliable measurements of properties including metallicity and ionization parameter of LAEs at high redshifts, we have carried out a large survey for  $z = 2.2$  LAEs, using our custom narrowband filter NB387 with Subaru/Suprime-Cam. At  $z = 2.2$ , important nebular lines such as [O II] $\lambda$ 3727, H $\beta$ , [O III] $\lambda$ 5007, 4959, H $\alpha$ , [N II] $\lambda$ 6584, are observable from the ground. Initial results were based on using three narrowbands to detect Ly $\alpha$ , [O II], and H $\alpha$  over the same volumes (Nakajima et al. 2012; see also Lee et al. 2012 and Ly et al. 2011 for the two NIR narrowbands and the NewH $\alpha$  Survey).

In this paper, we present results from NIR spectroscopy. We used Keck/NIRSPEC and Magellan/MMIRS spectrographs, and successfully detected H $\alpha$  emission from seven LAEs. The number is double the previous number of high- $z$  LAEs with NIR spectra (two from Finkelstein et al. 2011 and two from McLinden et al. 2011), and allows us to begin to examine statistical variation of rest-frame optical spectroscopic properties of LAEs at  $z \sim 2$ . Our first NIR spectroscopic

result discusses the kinematics of LAEs and is presented in Hashimoto et al. (2012). As a companion study, this paper presents the ionization and chemical properties of LAEs based on multiple nebular lines. Remarkably, we detected [O II] and [O III] lines from two LAEs, which provide ionization parameter estimates for LAEs for the first time. In addition, the oxygen lines allow us to determine oxygen abundances that compliment the previous spectroscopic constraints on metallicity of LAEs from the [N II]/H $\alpha$  index.

We also investigate Ly $\alpha$  and H $\alpha$  hydrogen lines for LAEs. A comparison of observed Ly $\alpha$ /H $\alpha$  ratios with the Case B recombination value (Ly $\alpha$ /H $\alpha$  = 8.7; Brocklehurst 1971) provides important insights into the physical mechanisms causing the strong Ly $\alpha$  emission in LAEs. Furthermore, we study Ly $\alpha$  and H $\alpha$  equivalent widths which probe star-formation history, stellar age, and metallicity.

This paper is organized as follows. We describe the data in §2. The detection and measurement of emission lines in the NIR spectroscopy is summarized in §3. In §4, we derive properties of LAEs including estimates of ionization parameter, metallicity, and SFR from the rest-frame optical nebular lines. We also check for the presence of active galactic nuclei (AGN) in the LAEs. In §5, we compare LAEs with other galaxies in terms of their ionization state, metallicity, and SFR. We then discuss the implications. We also discuss the physical properties inferred from Ly $\alpha$  and H $\alpha$  emission. We conclude the paper in §6 with a summary. Throughout this paper, magnitudes are given in the AB system (Oke 1974), and we assume a standard  $\Lambda$ CDM cosmology with  $(\Omega_m, \Omega_\Lambda, H_0) = (0.3, 0.7, 70 \text{ km s}^{-1} \text{ Mpc}^{-1})$ .

## 2. NIR SPECTROSCOPIC DATA

### 2.1. Sample Construction

We carried out NB387 imaging observation with Subaru/Suprime-Cam (Miyazaki et al. 2002) on 2009 December 14-16 and 19-20 to search for  $z = 2.2$  LAEs. A total of  $\sim 1.5$  square degrees are covered, with pointings in the following five fields: the Subaru/*XMM-Newton* Deep Survey (SXDS) field (Furusawa et al. 2008), the COSMOS field (Scoville et al. 2007), the Chandra Deep field South (CDFs; Giacconi et al. 2001), the Hawaii Hubble Deep Field North (HHDFN; Capak et al. 2004), and the SSA22 field (e.g., Steidel et al. 2000). The first results of the NB387 survey in the SXDS field have been presented in Nakajima et al. (2012). For the other fields, we select  $z = 2.2$  LAE candidates in the same manner as presented in Nakajima et al. (2012), and a summary of the full  $\sim 1.5$  square degrees survey will be presented elsewhere (K. Nakajima et al. in preparation). Briefly, objects which are bright in NB387 compared to the *U* and *B* bands are selected as LAE candidates. Interlopers such as [O II] emitters, CIV emitters, or active galactic nuclei (AGNs) are removed from the catalog by using UV, X-ray and/or radio data.

Seven candidates were selected for NIRSPEC follow-up. We selected COSMOS-13636, COSMOS-30679, and COSMOS-43982, since their Ly $\alpha$  spectra had been obtained with Magellan/MageE (M. Rauch et al. in preparation). COSMOS-08501, HHDFN-18325, and HHDFN-18431 were selected because of their large Ly $\alpha$  equiva-

TABLE 1  
SUMMARY OF THE LAE SAMPLE WITH NIR SPECTROSCOPY

Object	R.A.	Decl.	NB387	$U-NB387$	$B-NB387$	EW(Ly $\alpha$ )	$F(Ly\alpha)$	EXPTIME <sup>(6)</sup>			Instr.
	(1)	(1)	(2)	(3)	(3)	(4)	(5)	(J)	(H)	(K)	(7)
COSMOS-08501	10:01:16.80	+02:05:36.26	23.94	1.41 $\pm$ 0.09	2.05 $\pm$ 0.10	255 $\pm$ 26	24.0 $\pm$ 1.1	...	...	3600	N
COSMOS-13636	09:59:59.38	+02:08:38.36	23.53	0.91 $\pm$ 0.05	1.03 $\pm$ 0.06	73 $\pm$ 5	32.4 $\pm$ 1.4	...	...	5400	N
COSMOS-30679	10:00:29.81	+02:18:49.00	23.63	0.86 $\pm$ 0.05	0.55 $\pm$ 0.06	34 $\pm$ 3	19.1 $\pm$ 1.4	5400	7200	6300	N
COSMOS-30679 <sup>(†)</sup>	...	...	23.73	1.20 $\pm$ 0.07	1.16 $\pm$ 0.07	87 $\pm$ 7	23.2 $\pm$ 1.8	...	...	...	...
COSMOS-43982	09:59:54.39	+02:26:29.96	23.83	1.14 $\pm$ 0.08	1.30 $\pm$ 0.07	105 $\pm$ 8	30.3 $\pm$ 1.3	...	...	3600	N
HHDFN-18325	12:36:23.36	+62:06:05.10	21.84	1.26 $\pm$ 0.02	1.50 $\pm$ 0.02	122 $\pm$ 2	125. $\pm$ 1.2	...	...	3600	N
HHDFN-18431	12:36:25.62	+62:05:37.43	23.20	1.15 $\pm$ 0.03	1.71 $\pm$ 0.04	156 $\pm$ 6	37.8 $\pm$ 0.7	...	...	3600	N
CDFS-3865	03:32:32.31	-28:00:52.20	22.29	1.42 $\pm$ 1.23	1.01 $\pm$ 0.42	64 $\pm$ 29	84.0 $\pm$ 13.9	5100	10800		N/M
CDFS-6482	03:32:49.34	-27:59:52.35	23.26	1.47 $\pm$ 1.92	0.96 $\pm$ 0.66	75 $\pm$ 52	41.9 $\pm$ 22.0	...	10800		M
SSA22-8043	22:17:47.33	+00:08:28.36	24.51	0.66 $\pm$ 0.06	0.52 $\pm$ 0.06	28 $\pm$ 4	6.3 $\pm$ 1.1	...	10800		M

NOTE. — (1) Coordinates are in J2000. (2) NB387 aperture magnitude. The diameter of the aperture is 2''0, and the typical error is 0.04 mag. (3)  $u^*(U)-NB387$  and  $B-NB387$  colors and their  $1\sigma$  errors calculated from aperture magnitudes. (4) Rest-frame EW of Ly $\alpha$  emission line in units of  $\text{\AA}$  calculated from  $B-NB387$  color and redshift of H $\alpha$ . For HHDFN objects whose H $\alpha$  are not detected, we assume  $z = 2.18$ , which corresponds to the wavelength of the peak of the NB387 transmission curve. (5) Flux of Ly $\alpha$  emission line in units of  $10^{-17} \text{ erg s}^{-1} \text{ cm}^{-2}$  calculated from EW(Ly $\alpha$ ) and  $B$  band total magnitude. (6) Exposure time with NIRSPEC  $J$ ,  $H$ , and  $K$  bands in units of second. For the CDFS and SSA22 objects, their  $H$  and  $K$  bands spectra were taken with MMIRS using the  $HK$  grism. (7) Instrument used for the spectroscopy. "N" stands for NIRSPEC, and "M" for MMIRS. For CDFS-3865, its  $J$  band spectrum was obtained with NIRSPEC, and  $H$  and  $K$  bands spectra with MMIRS. (†) Values obtained after removing the contribution from an adjacent object (§4.2).

lent widths and fluxes measured from the NB387 imaging data. CDFS-3865, whose rest-frame optical spectrum has in part already been taken with MMIRS, was also observed with NIRSPEC for its [O II] detection. Table 1 summarizes the details of the sample.

For the MMIRS observation, we observed CDFS and SSA22 fields with one mask each. Details of the observation and data reduction procedures are presented in Hashimoto et al. (2012). Briefly, we found three LAEs in which we identified H $\alpha$  emission. In this paper, we make use of the spectra of the three LAEs; CDFS-3865, CDFS-6482, and SSA22-8043 (Table 1). Figure 1 shows the distributions of the LAEs presented in this paper on the  $U-NB387$  versus NB387 color magnitude diagram.

## 2.2. NIRSPEC Observation

The observations were carried out on 9–10 February 2011. Both nights were photometric. We observed in low-resolution mode, with a slit width of 0''76 and a slit length of 42''<sup>11</sup>. We observed all six candidate with Nirspec-6 filter (hereafter referred to as  $K$  band). In addition, we observed COSMOS-30679 with Nirspec-5 ( $H$  band) and Nirspec-3 ( $J$  band), and CDFS-3865 with  $J$  band. The wavelength ranges of  $K$ ,  $H$ , and  $J$  bands are 1.88–2.31  $\mu\text{m}$ , 1.47–1.76  $\mu\text{m}$ , and 1.15–1.36  $\mu\text{m}$ , respectively for our configurations. The resolution in the  $K$  band is  $R \sim 1500$ . Exposure times for each object are given in Table 1.

Our science targets were acquired using the invisible object acquisition procedures. In this mode, an alignment star brighter than  $K_{\text{Vega}} \sim 18$  was placed in the slit simultaneously with a science target. We first acquired the star at the center of the slit, then we nodded the telescope so that both the science target and the star were on the slit with the same distance from the slit center. For CDFS-3865 and HHDFN-18431, since we could not find any stars to place on the slit along with them, we first acquired the nearest star to the target (at distances of 68'' for CDFS-3865 and 39'' for HHDFN-18431), then

nodded the telescope with an offset, which was calculated from the WCS difference between the star and the science target. For HHDFN-18325, although a star was found at a distance of 32'', which is smaller than the slit length, half of the observation was done without the star in order to avoid the persistence caused by the previous target alignment star. During an exposure, we manually guided the slit using the slit-viewing camera; if the star started to drift out of the slit, we manually moved the slit so that the star (and thus the invisible science target) stayed in the slit throughout each exposure.

Standard stars, which were selected from the Hipparcos catalog to have A0V spectral type and similar airmass to the science targets, were observed at the beginnings and the ends of the nights. The calibration data were taken in an ABBA position pattern, while the science data in AB position pattern.

## 2.3. NIRSPEC Data Reduction

We used the Keck IRAF-based WMKONSPEC package<sup>12</sup> to reduce the data. We also used IRAF scripts that were originally written for reducing near-infrared multi-object spectroscopic data from Subaru/MOIRCS (MCSMDP; Yoshikawa et al. 2010).

The data reduction process included bias subtraction, flat fielding, distortion correction, wavelength calibration, cosmic ray rejection, (A-B) sky subtraction, residual background subtraction, image shifting, and stacking. We used the bias and flat data that were obtained in the same night as the science data. We performed wavelength calibration using OH-lines by comparing them with an OH-line list (Rousselot et al. 2000). For cosmic ray rejection, we used *LA.COSMIC* (van Dokkum 2001). The sky and OH-lines of an A-position image were roughly removed by subtracting an average B-position image created from the previous and following images. We then removed the residual sky by subtracting a 9-th order polynomial fit in the spatial direction after masking columns of positive and negative parts caused by the alignment star and the object. Individual images

<sup>11</sup> The effective slit length is  $\sim 38''$ , since we did not place objects in  $< 2''$  from the edges of the slit.

<sup>12</sup> <http://www2.keck.hawaii.edu/inst/nirspec/wmkonspec.html>

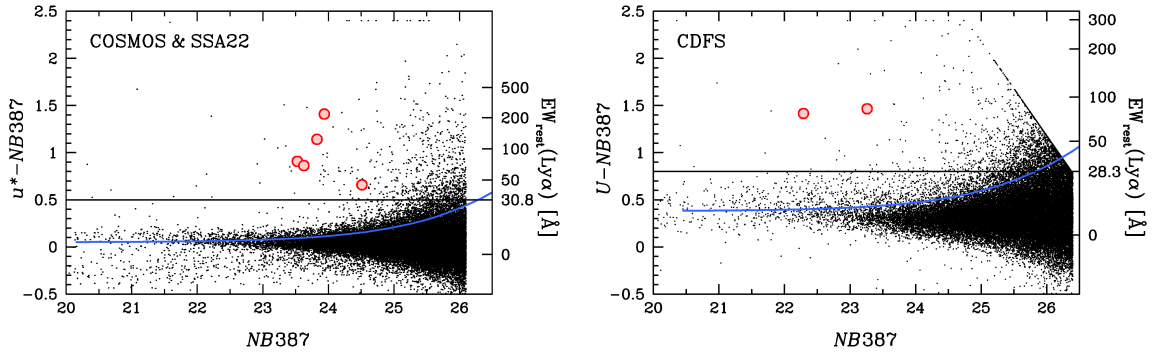


FIG. 1.— Distribution of all objects in the  $u^*(U)$ –NB387 vs. NB387 plane detected in the COSMOS and SSA22 fields (left) and in the CDFS field (right). The red circles show the LAEs presented in this paper, and the black dots show the NB387-detected objects. For the purpose of display, objects whose  $u^*(U)$ –NB387 colors exceed 2.4 are plotted at  $u^*(U)$ –NB387 = 2.4. The horizontal solid line in each panel shows the selection threshold of  $u^*(U)$ –NB387 and the blue curve indicates the  $2\sigma$  photometric error in  $u^*(U)$ –NB387 for objects with  $u^*$ –NB387 = 0.05 ( $U$ –NB387 = 0.38), which is the average  $u^*(U)$ –NB387 color of all the objects. The right  $y$ -axis in each panel shows the rest-frame Ly $\alpha$  equivalent width of  $z = 2.18$  LAEs with the  $u^*(U)$ –NB387 color corresponding to the left  $y$ -axis.

TABLE 2  
FLUXES OF NEBULAR LINES DETERMINED FROM NIR SPECTROSCOPY

Object	[O II] $\lambda$ 3727	H $\beta$	[O III] $\lambda$ 4959	[O III] $\lambda$ 5007	H $\alpha$	[N II] $\lambda$ 6484
COSMOS-08501	...	...	...	...	$1.91 \pm 0.36$	$< 0.36$
COSMOS-13636	...	...	...	...	$2.71 \pm 0.38$	$< 0.38$
COSMOS-30679	$1.04 \pm 0.26$	... (†)	... (†)	$4.11 \pm 0.41$	$3.11 \pm 0.27$	$< 0.27$
COSMOS-43982	...	...	...	...	$6.63 \pm 0.58$	$4.14 \pm 0.58$
Composite <sup>(*)</sup>	...	...	...	...	$2.64 \pm 0.20$	$< 0.20$
CDFS-3865	$2.53 \pm 0.41$	$13.0 \pm 4.1$	$19.0 \pm 3.5$	$53.6 \pm 3.5$	$38.5 \pm 2.4$	$< 2.4$
CDFS-6482	...	...	...	$23.8 \pm 2.7$	$9.38 \pm 1.71$	$< 1.71$
SSA22-8043	...	...	...	$11.0 \pm 4.2$	$14.7 \pm 4.3$	$< 4.3$

NOTE. — Fluxes and their  $1\sigma$  errors are given in unit of  $10^{-17}$  ergs $^{-1}$  cm $^{-2}$ . For lines with less than the  $3\sigma$  detection level, we list their  $1\sigma$  upper-limits. (\*) Composite spectrum of the four objects (§4.1). (†) These lines suffer badly from OH-lines subtraction errors.

were shifted in spatial direction so that the object is in the same position both in A-position and B-position images. The offset values were derived from the position differences of the alignment stars. When no star was observed simultaneously, we defined the offset values as the nod separation size. Finally, we stacked the position-matched individual images to create the two-dimensional (2D) spectra.

We obtained flux solutions by comparing spectra of the A0V standard stars and a model, which was created by a stellar spectral synthesis program (SPECTRUM; Gray & Corbally 1994) based on the Kurucz (1993)’s atmosphere models. The model spectra were then normalized so that their  $J$ ,  $H$ , and  $K$  band magnitudes matched with those of standard stars, whose photometry was obtained from the Two Micron All Sky Survey (2MASS) All-Sky Point Source Catalog. The one-dimensional (1D) spectra were extracted by summing up 6–10 pixels in the spatial direction. The lengths of columns were determined based on the seeing conditions; about two times the seeing size was used. We also confirmed that the sizes were large enough to detect most of the signal, and maximize the signal-to-noise (S/N) ratio. The 1D and 2D spectra are shown in Figure 2. We note in addition that the science targets and the standard stars used for the flux calibrations were observed and reduced with almost the same conditions, thus effects of slit losses were also corrected in the procedures, since the standard spec-

tra extracted in the procedure were normalized to have the total magnitude of that star. LAEs typically have half-light radii  $\lesssim 1.5$  kpc ( $\lesssim 0''.18$  at  $z = 2.2$ ; Bond et al. 2009), which is much smaller than the seeing size. Therefore, we cannot resolve LAEs with our observations, and assuming the PSF profile for the LAEs is reasonable.

Emission line fluxes were measured by fitting a Gaussian profile to each line with the IRAF task `splot`. The sky noise level was estimated in the following manner; we prepared an aperture box, which had approximately twice the seeing size in spatial direction and twice the FWHM of the best fit Gaussian to the emission line in wavelength direction. We spread more than 100 aperture boxes around the emission line after masking pixels heavily contaminated by OH-lines, and measured their photon counts. We then fit the histogram of the counts with a Gaussian, and regarded its  $\sigma$  as the  $1\sigma$  fluctuation for the aperture used to measure the emission line. The line fluxes and their  $1\sigma$  errors are summarized in Table 2.

### 3. EMISSION LINE DETECTIONS

#### 3.1. H $\alpha$ detection

We detect significant H $\alpha$  emission in  $K$  band 2D spectra for COSMOS-08501, COSMOS-13636, COSMOS-30679, COSMOS-43982, CDFS-3865, CDFS-6482, and SSA22-8043, but we do not identify any emission lines for the other two LAEs, HHDFN-18325 and HHDFN-18431. Both LAEs are expected to have strong Ly $\alpha$ ,

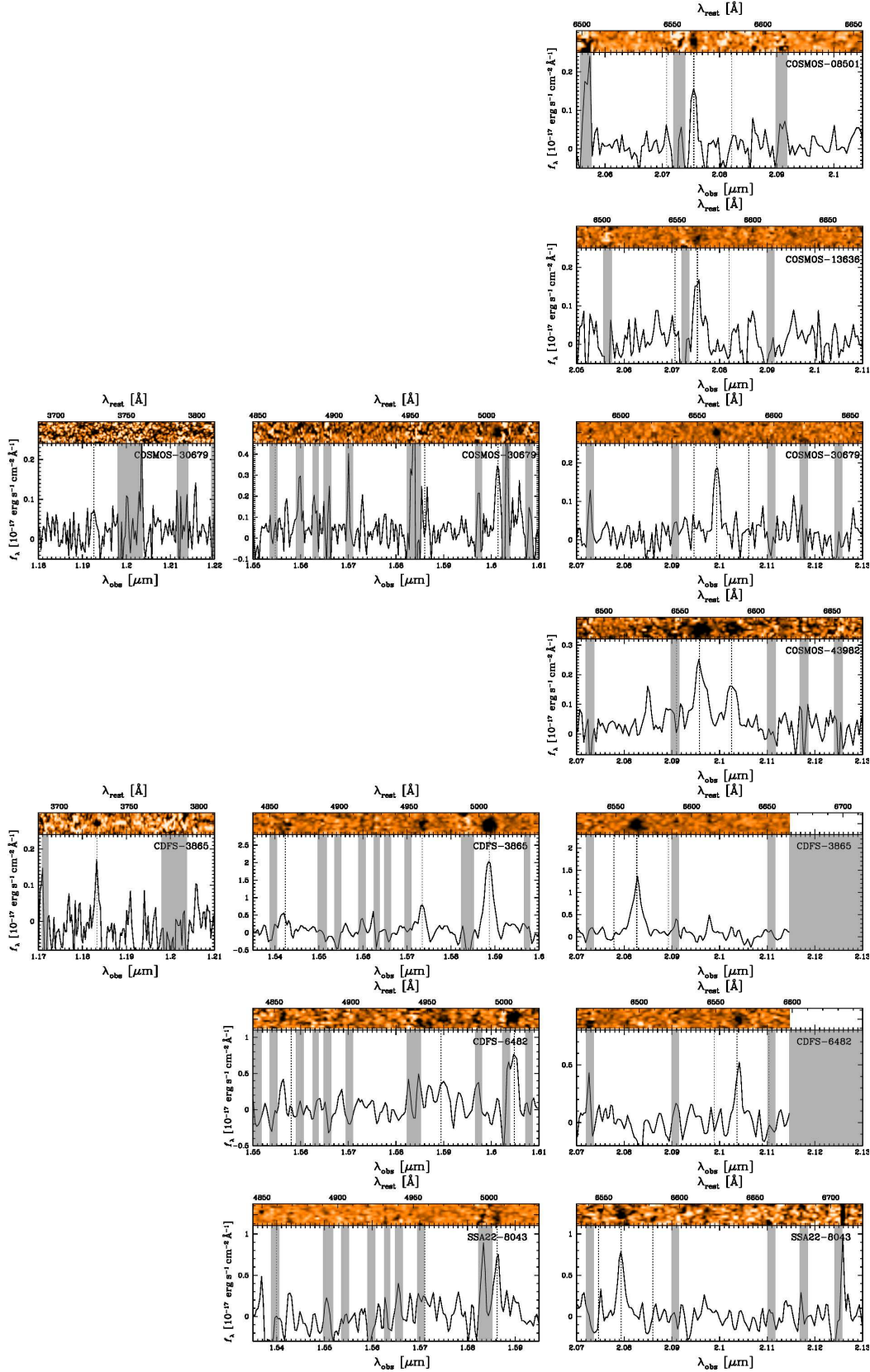


FIG. 2.— From left to right, the  $J$ ,  $H$ , and  $K$  band spectra of the LAEs. In each panel, the 2D and 1D spectra are shown in the top and bottom, respectively. The vertical dotted lines in the 1D spectra show the expected locations of nebular emission lines;  $[\text{O II}]\lambda 3727$ ,  $\text{H}\beta$ ,  $[\text{O III}]\lambda\lambda 4959, 5007$ ,  $[\text{N II}]\lambda 6548$ ,  $\text{H}\alpha$ , and  $[\text{N II}]\lambda 6584$ . The gray shaded areas overlaid on each 1D spectrum highlight spectral regions strongly affected by OH-airglow. For CDFS objects, their  $K$  band spectra at  $2.115 \mu\text{m}$  and longer are not obtained due to out of sensitivity of MMIRS, and also shaded with gray.



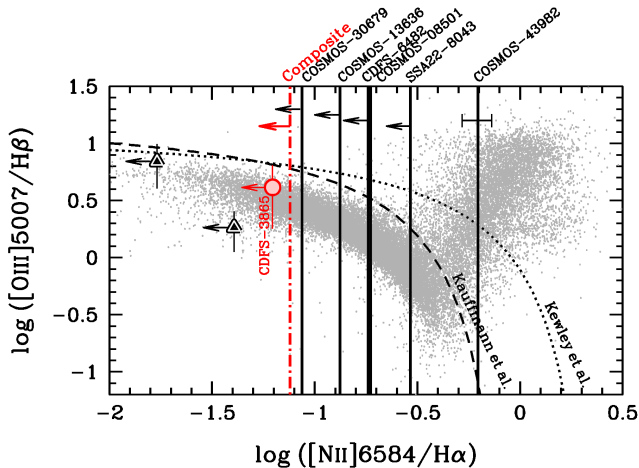


FIG. 3.— BPT-diagram (Baldwin et al. 1981). The dotted and dashed curves show the dividing line between star-forming galaxies and AGNs defined by Kewley et al. (2001) and Kauffmann et al. (2003), respectively. CDFS-3865 is shown with the red circle, while the other LAEs are shown with the vertical solid lines, due to the lacks of [O III] and/or H $\beta$ . Since we do not identify [N II] except for COSMOS-43982, upper-limits of [N II]/H $\alpha$  are given. The [N II]/H $\alpha$  ratio for COSMOS-43982 is given with a horizontal error bar. The red dot-dashed vertical line indicates the upper-limit of [N II]/H $\alpha$  for the composite spectrum of NIRSPEC-detected LAEs. The two triangles represent LAEs at  $z \sim 2.3$  and  $2.5$  from Finkelstein et al. (2011). The gray small points are randomly selected objects from the SDSS spectroscopic sample.

hence strong H $\alpha$ . A possible reason why we do not detect lines for HHDFN-18431 is that no alignment star was observed simultaneously, and the object may have drifted significantly out of the slit. The same issue may explain the non-detection of H $\alpha$  for HHDFN-18325, since half of the observation was done without an alignment star (§2.2). Since we have not yet obtained Ly $\alpha$  spectra for the two objects, the non-detections may be alternatively due to the mis-selection of LAEs. Future optical spectroscopy is needed to resolve this issue. In the following sections, we use the seven LAEs with reliable H $\alpha$  detection.

### 3.2. Other emission line detections

For CDFS-3865, we additionally obtain [O II] $\lambda$ 3727, H $\beta$ , and [O III] $\lambda$ 4959, 5007 emission lines. Combined with the H $\alpha$ -detection, a full suite of prominent rest-frame optical nebular lines are thus obtained for this object. For COSMOS-30679, we obtain [O II] and [O III] $\lambda$ 5007 emission lines, while we do not identify H $\beta$  and [O III] $\lambda$ 4959, because they fall in a dense OH-line wavelength range. We thus cannot place meaningful upper limits on their fluxes. When fluxes for these lines are required for inferring physical properties, we assume a value of 0.28 for the [O III] $\lambda$ 4959/5007 ratio and calculate the H $\beta$  flux based on the observed H $\alpha$  flux, the intrinsic H $\alpha$ /H $\beta$  ratio assuming Case B recombination (2.86; Osterbrock 1989), and the dust extinction estimated from SED fitting. We emphasize that the two LAEs, CDFS-3865 and COSMOS-30679, are the first [O II]-detected LAEs individually at high- $z$ . The [O II]+[O III] lines provide the simultaneous determinations of ionization state and oxygen abundance (§4.3).

For CDFS-6482 and SSA22-8043, we detect [O III] $\lambda$ 5007 while we do not identify H $\beta$  and [O III] $\lambda$ 4959,

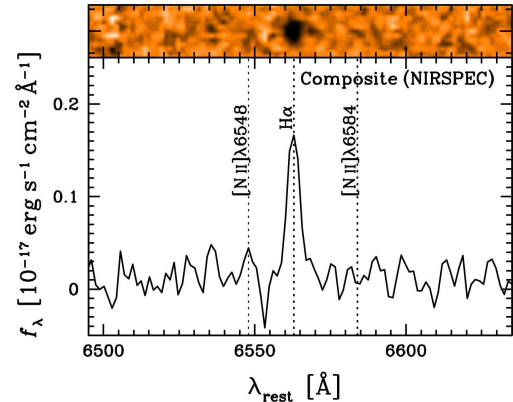


FIG. 4.— K band composite spectrum of the NIRSPEC-detected objects.

probably due to the contamination by OH-lines and the limited sensitivity of the instrument (More detailed descriptions about the MMIRS objects are provided by Hashimoto et al. 2012). For COSMOS-43982, we clearly detect [N II] $\lambda$ 6584 emission line, which is not identified for the other LAEs. The [N II]-detection suggests a non-negligible contribution of AGN to the emission lines for the object. Further investigations of AGN contamination are discussed in §4.1.

## 4. PHYSICAL PROPERTIES OF LAES

### 4.1. Removal of objects with AGN

AGN, as well as star-formation, can produce large amounts of ionizing photons, and show strong Ly $\alpha$ . Since our interest is star-forming LAEs, we need to remove LAEs with AGN activity from the sample.

During the LAE sample selection, bright LAEs with AGN signature have been removed (see Nakajima et al. 2012). Obvious AGNs are therefore excluded from the sample. However, the procedure is not always perfect, and can miss objects with relatively weak AGN activity. In order to assess possible contamination of AGN in our LAE sample, we plot our LAEs on a BPT diagram (Figure 3; Baldwin et al. 1981) which is widely used to separate star forming galaxies from AGN. In Figure 3, the underlying small gray points denote the spectroscopic objects from the Sloan Digital Sky Survey (SDSS; York et al. 2000)<sup>13</sup>. The two curves shown in Figure 3 are the empirical demarcations (Kewley et al. 2001; Kauffmann et al. 2003). Since only one LAE, CDFS-3865, has both [O III] and H $\beta$ , all the other LAEs are shown with vertical lines. Due to the non-detection of [N II], the vertical lines show upper-limits of [N II]/H $\alpha$  except for COSMOS-43982, which has an individual [N II] detection. Based on its relatively high [N II]/H $\alpha$  ratio, COSMOS-43982 may be contaminated by an AGN, though there remains a possibility that this LAE may be a star-formation dominated galaxy with a very small [O III]/H $\beta$  ratio. For this analysis, we choose to be conservative and regard the object as a candidate possessing AGN activity. The properties of COSMOS-43982 are considered and interpreted carefully in the following sections.

<sup>13</sup> We use a part of the spectroscopic data taken from the MPA-JHU DR7 release of spectrum measurements: <http://www.mpa-garching.mpg.de/SDSS/DR7/>

TABLE 3  
BROADBAND PHOTOMETRY OF THE LAES

COSMOS sample <sup>(1)</sup>	<i>B</i>	<i>V</i>	<i>r'</i>	<i>i'</i>	<i>z'</i>	<i>J</i>	...	<i>K<sub>s</sub></i>	[3.6]	[4.5]	[5.8]	[8.0]
COSMOS-08501	25.86	25.91	26.08	25.88	25.81	98.45	...	25.64	99.99	99.99	99.99	99.99
COSMOS-13636	24.43	24.21	24.35	24.19	24.24	23.10	...	23.43	24.10	23.75	99.99	99.99
COSMOS-30679	24.05	23.12	22.91	22.46	22.33	21.15	...	21.82	22.12	22.57	99.99	23.06
COSMOS-30679 <sup>(†)</sup>	24.76	23.82	24.44	24.09	23.49	22.31	...	23.29	...	...	...	...
COSMOS-43982	25.00	24.38	24.48	23.99	23.73	21.89	...	21.62	21.20	21.02	20.69	20.75
(limitmag)	(29.13)	(28.18)	(28.33)	(27.87)	(26.89)	(24.17)	...	(24.84)	(25.05)	(24.25)	(21.90)	(20.63)
(limitmag) <sup>(†)</sup>	(28.76)	(26.24)	(25.79)	(25.34)	(24.85)	(23.68)	...	(24.63)	...	...	...	...
CDFS sample <sup>(2)</sup>	<i>B</i>	<i>V</i>	<i>R</i>	<i>I</i>	<i>z'</i>	<i>J</i>	<i>H</i>	<i>K</i>	[3.6]	[4.5]	[5.8]	[8.0]
CDFS-3865	23.01	22.94	22.92	23.14	22.93	22.73	22.27	22.38	22.82	22.82	22.51	23.00
CDFS-6482	23.93	23.87	23.78	23.95	23.67	23.50	23.36	23.07	22.88	22.83	22.34	99.99
(limitmag)	(28.32)	(27.85)	(27.82)	(26.14)	(25.64)	(24.57)	(24.57)	(23.97)	(26.23)	(25.68)	(23.66)	(23.43)
SSA22 sample <sup>(3)</sup>	<i>B</i>	<i>V</i>	<i>R</i>	<i>i'</i>	<i>z'</i>	<i>J</i>	...	<i>K</i>	[3.6]	[4.5]	[5.8]	[8.0]
SSA22-8043	24.80	24.63	25.54	24.64	24.59	24.10	...	21.79	23.33	23.14	26.58	21.15
(limitmag)	(27.85)	(27.99)	(28.03)	(27.75)	(27.16)	(24.74)	...	(22.78)	(25.40)	(23.64)	(22.71)	(20.95)

NOTE. — Broadband photometry of the LAEs. All magnitudes are total magnitudes. 99.99 mag means no signal detected. Magnitudes in parentheses are  $1\sigma$  uncertainties adopted in SED fitting.

<sup>(1)</sup> *BVR'i'z'* data are obtained from Subaru/Suprime-Cam, *J* data from UKIRT/WFCAM, *K<sub>s</sub>* data from CFHT/WIRCAM, and [3.6] – [8.0] data from Spitzer/IRAC. All data are collected from the COSMOS Archive.

<sup>(2)</sup> *BVRI* data are obtained from MPG/ESO 2.2m/WFI, *z'* data from CTIO/MOSAIC II, *JK* data from CTIO/ISPI, *H* data from NTT/SOFI, and [3.6] – [8.0] data from Spitzer/IRAC. Optical and NIR data are collected from the MUSYC Public Data Release (Gawiser et al. 2006), and Spitzer data from the SIMPLE Legacy II project.

<sup>(3)</sup> *BVRi'z'* data are obtained from Subaru/Suprime-Cam, *J* data from KPNO/NEWFIRM, *K* data from UKIRT/WFCAM, and [3.6] – [8.0] data from Spitzer/IRAC. Optical data are provided by T. Hayashino (see also Hayashino et al. 2004), *J* data are obtained from the NewH $\alpha$  survey (Ly et al. 2011; Lee et al. 2012). *K* data are collected from the WFCAM data access page, and Spitzer data from the Spitzer Heritage Archive.

<sup>(†)</sup> Values obtained after removing the contribution from an adjacent object (§4.2). The limiting magnitudes are calculated by adding the photometric errors and additional errors (residuals after subtracting GALFIT models) in quadrature. The limiting magnitudes are thus shallower than those given above (photometric only).

For CDFS-3865, thanks to its relatively strong constraint on [N II]/H $\alpha$ , we can see that the object is along the star forming sequence and has negligible AGN activity, similar to two other LAEs with spectroscopic follow-up at similar redshifts (Finkelstein et al. 2011). Although the other LAEs have no constraint on their *y*-axis values, AGN contributions to them are assumed to be minimal, since there are few AGNs in the range  $\log([\text{N II}]/\text{H}\alpha) \lesssim -0.5$ , as suggested from the underlying SDSS galaxies. In order to check the assumption, we stack the *K* band spectra of the four NIRSPEC-detected LAEs<sup>14</sup> with inverse-variance weights. The composite spectrum is shown in Figure 4, and provides an average, deeper constraint on [N II]/H $\alpha$  ratio for the LAEs. The red dot-dashed line in Figure 3 shows the upper-limit of [N II]/H $\alpha$  ratio constrained by the composite spectrum. The line is further away from the area occupied with AGNs. Therefore, AGN activity is on average negligible for the LAEs. In the following sections, we regard all the LAEs except for COSMOS-43982 as galaxies dominated by star-formation.

#### 4.2. Stellar Mass and $E(B-V)$ from SED fitting

We perform SED fitting to broadband photometry to infer properties of the stellar populations. The majority of images are collected from publicly available databases (see notes in Table 3). The optical and NIR photometry is done with a 2'' diameter aperture using the double-image mode of SExtractor (Bertin & Arnouts 1996). The aperture magnitudes are then converted

into total magnitudes using aperture correction values, which are estimated from differences between aperture magnitudes and MAG\_AUTO values for point sources. For the IRAC imaging, we use a 3'' diameter aperture and Yan et al. (2005)'s aperture correction values. Table 3 summarizes the results.

The procedure of the SED fitting is the same as that of Ono et al. (2010), except for fixed redshifts, which are derived from H $\alpha$ . Briefly, we use the stellar population synthesis model GALAXEV (Bruzual & Charlot 2003) for stellar SEDs, and include nebular emission (Schaerer & de Barros 2009). A Salpeter initial mass function (IMF; Salpeter 1955) is assumed. We choose constant star-formation history and the stellar metallicity  $Z = 0.2 Z_{\odot}$ . For dust extinction, we use Calzetti's extinction law (Calzetti et al. 2000) on the assumption of  $E(B-V)_{\text{gas}} = E(B-V)_{\star}$  as proposed by Erb et al. (2006b), although this assumption is still debatable for high-*z* galaxies (e.g., Förster Schreiber et al. 2009; Ly et al. 2012). Intergalactic medium (IGM) attenuation is calculated using the prescription given by Madau (1995). These assumptions are usually used for SED fitting for high-*z* LAEs. E.g, Guaita et al. (2011) test three different star-formation histories when performing SED fitting to  $z \sim 2.1$  stacked LAEs, and find equally good fits to the data. The authors also note that SED fitting can relatively well constrain stellar mass and dust extinction among the free parameters. The derived properties are given in Table 4, and the best-fit SEDs are shown in Figure 5.

One problem is that COSMOS-30679 was found to be blended with another brighter adjacent object via examination of the COSMOS HST/ACS F814W imaging data

<sup>14</sup> We do not use the MMIRS spectra due to their worse sensitivity and spectral resolution.

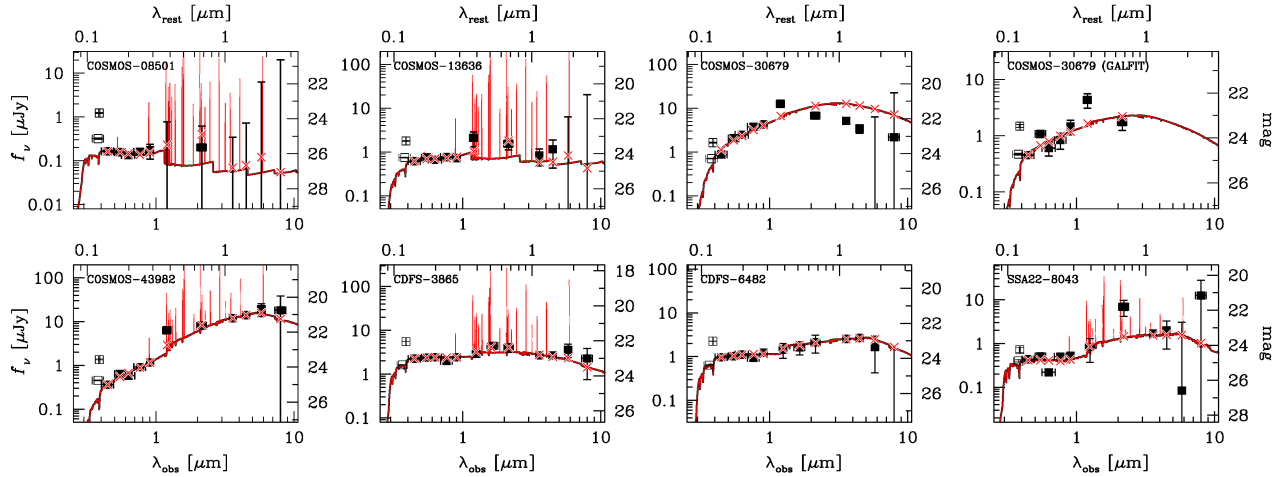


FIG. 5.— Results of SED fitting. The filled squares show the observed flux densities used for the fitting ( $B$ ,  $V$ ,  $r$ ,  $i$ ,  $z$ ,  $J$ ,  $H$ ), ( $K$ , [3.6], [4.5], [5.8], and [8.0]), while the open squares indicate those we omit for the fitting ( $U$  and NB387), due to the unknown flux contributions of IGM absorption. The red lines show the best-fit model spectra, and the red crosses correspond to the best-fit flux densities.

TABLE 4  
PHYSICAL PROPERTIES FROM SED FITTING

Object	$f_{\text{esc}}^{\text{ion}}$	$\log(M_*)$ ( $M_{\odot}$ )	$E(B - V)$ (mag)	$\log(\text{age})$ (yr)	$\log(\text{SFR})$ ( $M_{\odot}/\text{yr}$ )	$\chi^2$
COSMOS-08501	$0.0^{+1.0}_{-0.0}$	$7.82^{+1.23}_{-0.28}$	$0.08^{+0.11}_{-0.08}$	$6.44^{+2.47}_{-1.34}$	$1.38^{+1.91}_{-1.14}$	1.821
COSMOS-13636	$0.7^{+0.1}_{-0.5}$	$9.30^{+0.08}_{-0.33}$	$0.27^{+0.02}_{-0.08}$	$6.18^{+1.20}_{-1.08}$	$3.12^{+1.16}_{-1.28}$	21.162
COSMOS-30679	$1.0^{+0.0}_{-0.0}$	$11.14^{+0.00}_{-0.00}$	$0.63^{+0.00}_{-0.00}$	$6.42^{+0.00}_{-0.00}$	$4.72^{+0.00}_{-0.00}$	2391.029
COSMOS-30679(†)	$1.0^{+0.0}_{-0.0}$	$10.30^{+0.12}_{-0.15}$	$0.53^{+0.03}_{-0.03}$	$6.42^{+0.08}_{-1.32}$	$3.88^{+1.44}_{-0.23}$	19.769
COSMOS-43982	$0.2^{+0.1}_{-0.2}$	$10.73^{+0.08}_{-0.00}$	$0.43^{+0.00}_{-0.04}$	$8.31^{+0.25}_{-0.00}$	$2.50^{+0.00}_{-0.16}$	71.371
CDFS-3865	$0.7^{+0.1}_{-0.1}$	$9.50^{+0.03}_{-0.02}$	$0.18^{+0.01}_{-0.01}$	$7.02^{+0.06}_{-0.04}$	$2.49^{+0.05}_{-0.06}$	16.854
CDFS-6482	$1.0^{+0.0}_{-0.3}$	$9.72^{+0.09}_{-0.07}$	$0.18^{+0.03}_{-0.02}$	$7.86^{+0.20}_{-0.23}$	$1.92^{+0.15}_{-0.11}$	4.986
SSA22-8043	$0.0^{+0.4}_{-0.0}$	$10.07^{+0.07}_{-0.06}$	$0.03^{+0.02}_{-0.01}$	$9.44^{+0.00}_{-0.10}$	$0.76^{+0.07}_{-0.03}$	112.152

NOTE. — Physical properties and their  $1\sigma$  errors of LAEs from SED fitting. Stellar metallicity is fixed to  $0.2 Z_{\odot}$ . The second column ( $f_{\text{esc}}^{\text{ion}}$ ) shows the escape fraction of ionizing photons (a free parameter). (†) Values obtained after removing the contribution from an adjacent object (§4.2).

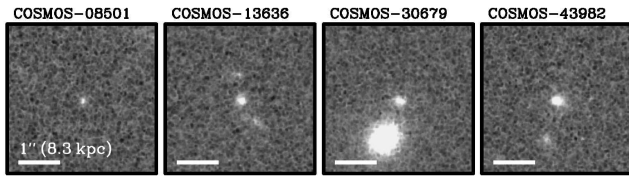


FIG. 6.— HST/ACS F814W images for COSMOS objects. White tick indicates 1 arcsec, corresponding to  $\sim 8.3$  kpc at  $z = 2.2$ . North is up and east is to the left.

(Figure 6). In order to deblend this object, we use the galaxy profile fitting software GALFIT (v3.0; Peng et al. 2010). We first run GALFIT in the  $B$  band and fit both objects simultaneously. Then, we perform fittings in other bands by fixing parameters (except for brightnesses) to those derived in the  $B$  band fitting and derive the deblended photometry, which is listed in Table 4. We confirm that the  $i'$  band brightness estimated from the deblended object is consistent with the photometry in the HST/ACS F814W high-resolution image within their errors. We add residuals after subtracting the fitted profiles into the photometric errors in quadrature, so that those errors are used in the SED fitting. Since the adjacent object appears dominant at longer wavelengths and deblending gets less reliable, we do not perform the

deblending for the IRAC images. The best fit SEDs of COSMOS-30679 after and before deblending are shown in upper right two panels in Figure 5. Although the bumpy shape of the SED after the deblending suggests additional contamination from the adjacent object, the fitting is acceptable (relatively small  $\chi^2$  value) compared with that obtained before deblending. In the following sections, we use the quantities after deblending.

We obtain from our sample stellar masses ranging from  $7 \times 10^7 M_{\odot}$  to  $2 \times 10^{10} M_{\odot}$  (except for the AGN LAE) and dust extinction  $E(B - V) = 0.03$  to  $0.53$ . These results are consistent with the previously recognized trend that LAEs at  $z \sim 2$  are diverse, unlike higher redshift counterparts (e.g., Nilsson et al. 2011). We also find that dust extinctions estimated from the  $H\alpha/H\beta$  ratio and SED fitting are consistent with each other for CDFS-3865 (Hashimoto et al. 2012). This supports our assumption that the dust extinction from SED fitting can be reasonably applied for the extinction correction of nebular lines.

#### 4.3. Ionization Parameter and Metallicity



TABLE 5  
PHYSICAL PROPERTIES FROM THE NEBULAR LINES

Object	$12 + \log(\text{O}/\text{H})$		$q_{ion}$ ( $10^7 \text{ cm s}^{-1}$ )	SFR ( $M_{\odot} \text{ yr}^{-1}$ )	SFR <sub>cor</sub> ( $M_{\odot} \text{ yr}^{-1}$ )	EW(H $\alpha$ ) ( $\text{\AA}$ )	$L(\text{H}\alpha)$ ( $10^{42} \text{ erg s}^{-1}$ )	EW(Ly $\alpha$ ) ( $\text{\AA}$ )	$L(\text{Ly}\alpha)$ ( $10^{42} \text{ erg s}^{-1}$ )	AGN (10)
	$N2$ (1)	$R23$ (2)								
COSMOS-08501	< 8.73	...	...	$5.3^{+1.0}_{-1.0}$	$6.7^{+2.7}_{-2.1}$	> 280	$0.67 \pm 0.13$	$255 \pm 26$	$8.41 \pm 0.40$	0
COSMOS-13636	< 8.61	...	...	$7.5^{+1.1}_{-1.1}$	$17.3^{+2.6}_{-4.9}$	$93^{+26}_{-32}$	$0.95 \pm 0.13$	$73 \pm 5$	$11.35 \pm 0.50$	0
COSMOS-30679 <sup>(†)</sup>	< 8.70	8.08–8.67	3.4–15	$9.0^{+0.8}_{-0.8}$	$45.2^{+5.4}_{-5.4}$	$93^{+25}_{-33}$	$1.14 \pm 0.10$	$87 \pm 7$	$8.47 \pm 0.65$	0
COSMOS-43982	...	...	...	$19.0^{+1.7}_{-1.7}$	$71.2^{+6.2}_{-9.9}$	$41^{+4}_{-4}$	$2.41 \pm 0.21$	$105 \pm 8$	$11.00 \pm 0.47$	1
CDFS-3865	< 8.35	$7.84^{+0.24}_{-0.25}$	$24^{+20}_{-9}$	$107.9^{+6.7}_{-6.7}$	$190.0^{+12.9}_{-12.9}$	$813^{+175}_{-216}$	$13.65 \pm 0.85$	$64 \pm 29$	$29.79 \pm 4.93$	0
CDFS-6482	< 8.72	...	...	$27.2^{+5.0}_{-5.0}$	$48.0^{+9.6}_{-9.1}$	$261^{+103}_{-149}$	$3.45 \pm 0.63$	$75 \pm 52$	$15.40 \pm 8.09$	0
SSA22-8043	< 8.90	...	...	$41.0^{+12.0}_{-12.0}$	$44.5^{+13.2}_{-13.1}$	$120^{+53}_{-69}$	$5.19 \pm 1.52$	$28 \pm 4$	$2.22 \pm 0.38$	0

NOTE. — (1) Oxygen abundance derived from  $N2$ -index (§4.3). If [N II] is undetected,  $1\sigma$  upper-limit is given. (2) Oxygen abundance derived from  $R23$ -index (§4.3). Ionization parameter is derived at the same time. (3) Ionization parameter ( $10^7 \text{ cm s}^{-1}$ ) estimated from the [O III]/[O II] ratio and  $Z(R23)$  (§4.3). (4) Star formation rate ( $M_{\odot} \text{ yr}^{-1}$ ) derived from uncorrected H $\alpha$  luminosity (§4.4). (5) Star formation rate ( $M_{\odot} \text{ yr}^{-1}$ ) derived from H $\alpha$  luminosity after correcting for extinction derived from SED fitting (§4.4). (6) Rest-frame equivalent width of H $\alpha$  ( $\text{\AA}$ ; §4.5). (7) Observed luminosity of H $\alpha$  ( $10^{42} \text{ erg s}^{-1}$ ). (8) Rest-frame equivalent width of Ly $\alpha$  ( $\text{\AA}$ ; see Table §1). (9) Observed luminosity of Ly $\alpha$  ( $10^{42} \text{ erg s}^{-1}$ ). (10) Flag of AGN (§4.1): AGN candidates are flagged with "1". <sup>(†)</sup> Values obtained after removing the contribution from an adjacent object (§4.2). Since H $\beta$  and [O III] $\lambda 4959$  are inferred from other lines and thus involve large uncertainties, its metallicity (both  $N2$  and  $R23$ ) and ionization parameter are given with  $2\sigma$  uncertainties.

The ionization state in an HII region is often characterized by the ionization parameter,  $q_{ion}$ <sup>15</sup>, which is the ratio of the mean ionizing photon flux to the mean hydrogen atom density. Larger  $q_{ion}$  means the HII region is more highly ionized, followed by strong emission lines with higher ionization potentials. In this sense, the ionization parameter is well determined using ratios of emission lines of different ionization stages of the same element, such as the [O III]/[O II] ratio (e.g., Kewley & Dopita 2002). However, the [O III]/[O II] ratio depends not only on ionization state but also on gas metallicity (Fig. 1 of Kewley & Dopita 2002). Conversely, metallicity estimates using  $R23$ -index (Pagel et al. 1979):

$$R23 = \frac{[\text{O II}]\lambda 3727 + [\text{O III}]\lambda\lambda 5007, 4959}{\text{H}\beta} \quad (1)$$

are affected by the ionization parameter to some extent (e.g., Kewley & Dopita 2002; Nagao et al. 2006). Therefore, we combine the [O III]/[O II] ratio and  $R23$ -index (both corrected for dust extinction estimated from SED fitting) to estimate its ionization parameter and metallicity at the same time iteratively.

We describe the procedure for CDFS-3865 as an example. As an initial guess of metallicity, we use the empirical  $R23$  indicator determined by local galaxies (Maiolino et al. 2008). We obtain two solutions  $12 + \log(\text{O}/\text{H}) = 7.45^{+0.25}_{-0.19}$  and  $8.66^{+0.20}_{-0.26}$ . We then use another alternative indicator,  $N2$ -index defined as [N II] $\lambda 6584/\text{H}\alpha$  (Maiolino et al. 2008). The upper-limit of [N II]/H $\alpha$  provides an upper-limit of metallicity  $12 + \log(\text{O}/\text{H}) = 8.35$  ( $1\sigma$ ), which removes the high-metallicity solution by  $R23$ -index at the  $2.5\sigma$  level. Therefore, the empirical relation yields the metallicity  $12 + \log(\text{O}/\text{H}) = 7.45^{+0.25}_{-0.19}$ . As the second step, we use this metallicity and the [O III]/[O II] ratio to estimate its ionization parameter. Kewley & Dopita (2002) calculate the relations between [O III]/[O II] ratio and ionization

parameter with discrete values of metallicity. Among them, our initial guess of metallicity corresponds to their lowest metallicity ( $\sim 0.09 Z_{\odot}$ ; Allende Prieto et al. 2001). By using the relation, we find that the high [O III]/[O II] ratio can only be reproduced with ionization parameters as high as several times  $10^8 \text{ cm s}^{-1}$ . As the third step, we recalculate its metallicity from the Kewley & Dopita (2002)'s relation ( $R23$ -index) for the ionization parameter  $3 \times 10^8 \text{ cm s}^{-1}$ , and obtain  $12 + \log(\text{O}/\text{H}) = 7.84^{+0.24}_{-0.25}$ . Finally, we recalculate its ionization parameter based on the metallicity and Eq. (12) of Kewley & Dopita (2002)<sup>17</sup>, and obtain  $q_{ion} = 2.4^{+2.0}_{-0.9} \times 10^8 \text{ cm s}^{-1}$ . This is consistent with the assumed ionization parameter in the third step ( $3 \times 10^8 \text{ cm s}^{-1}$ ). We check that further iterations do not change our final solutions. To summarize, CDFS-3865 has the ionization parameter  $q_{ion} = 2.4^{+2.0}_{-0.9} \times 10^8 \text{ cm s}^{-1}$  and the metallicity  $12 + \log(\text{O}/\text{H}) = 7.84^{+0.24}_{-0.25}$ .

In the same manner, we estimate COSMOS-30679's ionization parameter and metallicity to be  $q_{ion} = (3.4\text{--}15) \times 10^7 \text{ cm s}^{-1}$  and  $12 + \log(\text{O}/\text{H}) = 8.08\text{--}8.67$ , respectively. Since COSMOS-30679 does not have H $\beta$ , its strength is inferred from H $\alpha$  assuming the Case B and the dust extinction. In addition, its broadband SED is fitted after being deblended with the adjacent object (§4.2). Therefore, the object may possess larger uncertainties. To be conservative, we adopt the  $2\sigma$  range as the uncertainty for its derived quantities. We check that the upper-limit of metallicity from the  $N2$ -index is consistent within the  $2\sigma$  level.

For the LAEs without [O II], we estimate their metallicities by using the empirical  $N2$ -index relation, and no constraint on ionization parameters is provided for them. The metallicities and the ionization parameters are summarized in Table 5.

#### 4.4. SFR

<sup>16</sup> Using the  $1.5 \times 10^8 \text{ cm s}^{-1}$  relation does not change the metallicity estimate significantly ( $\sim 0.02 \text{ dex}$  lower).

<sup>15</sup> We use the subscript "ion" for the ionization parameter to distinguish it from the  $q$ -parameter which stands for the effect of dust on Ly $\alpha$  compared with UV-continuum (§5.2.1).

<sup>17</sup> Although the original relations are suspended at  $q_{ion} = 3 \times 10^8 \text{ cm s}^{-1}$ , we extend their polynomials toward higher  $q_{ion}$  values.

The H $\alpha$  luminosity is thought to be the most reliable SFR indicator relative to those based on the rest-frame UV and optical spectral features. Indeed, it is proportional to the birth rate of massive stars as well as being relatively insensitive to dust extinction as compared with UV-continuum. We measure the SFR of the LAEs from the H $\alpha$  luminosity using the relation (Kennicutt 1998):

$$\text{SFR} [M_{\odot} \text{ yr}^{-1}] = 7.9 \times 10^{-42} L(\text{H}\alpha) \text{ erg s}^{-1}. \quad (2)$$

In Table 5, we summarize the derived SFRs.

#### 4.5. H $\alpha$ Equivalent Width

We calculate the H $\alpha$  equivalent width of an object from the H $\alpha$  flux divided by its continuum flux density derived from  $K$  band photometry. To estimate the proper continuum, however, we have to remove the contribution of the H $\alpha$  emission on the  $K$  band photometry. We follow the prescription given in the appendix of Guaita et al. (2010) (see also Finkelstein et al. 2011):

$$f_{\nu}(\text{H}\alpha) = R_T \times \frac{F(\text{H}\alpha)}{\int T_K(\lambda) \frac{c}{\lambda^2} d\lambda}, \quad (3)$$

where  $f_{\nu}(\text{H}\alpha)$  is the amount of flux that H $\alpha$  line contributes to the  $K$  band photometry,  $F(\text{H}\alpha)$  is the observed H $\alpha$  flux,  $R_T$  is the ratio between the filter transmission at  $\lambda_{\text{H}\alpha}$  and the maximum of the  $K$  band transmission function, and  $T_K(\lambda)$  is the  $K$  band filter transmission at a given wavelength. The flux estimated from the calculation is subtracted from the  $K$  band photometry. The corrections span from 0.05 (COSMOS-43982) to as much as 0.63 mag (CDFs-3865). Since COSMOS-08501 is not detected in the  $K$  band, we use the  $1\sigma$  lower-limit of the  $K$  band photometry. We thus obtain an upper-limit of the continuum (correction  $> 0.26$  mag), hence a lower-limit of the EW(H $\alpha$ ) for COSMOS-08501. The derived EWs(H $\alpha$ ) are listed in Table 5.

## 5. DISCUSSION

In this section, we discuss the physical properties of LAEs determined by this study in conjunction with Finkelstein et al. (2011) and Nakajima et al. (2012). In the first subsection, we make comparisons in terms of ionization parameter, metallicity, and SFR of LAEs at  $z \sim 2$  as well as lower-redshifts, and other galaxies at similar redshifts such as LBGs. We then examine the implications. In the second subsection, we show the properties of LAEs newly found by spectroscopy based on Ly $\alpha$  and H $\alpha$  hydrogen recombination lines. We extend the discussion to understanding the origins of the strong Ly $\alpha$  emission observed in LAEs.

### 5.1. Comparisons between LAEs and other galaxies

#### 5.1.1. Ionization State

We find high ionization parameters for the LAEs. In this section, we examine this point further by comparison to other galaxies, and discuss its implications.

The situation is most clearly seen in Figure 7, which shows the [O III]/[O II] ratio versus  $R23$ -index. We plot CDFS-3865 and COSMOS-30679 (red circles), and other galaxies such as LBGs at  $z = 2-3$  (blue symbols). The black grid represents model predictions of [O III]/[O II] ratio and  $R23$ -index at a given metallicity and (discrete)

ionization parameter (Kewley & Dopita 2002). According to the calculation, CDFS-3865 is close to the  $q_{ion} = 3 \times 10^8 \text{ cm s}^{-1}$  curve. This confirms its high ionization parameter and low oxygen abundance. The high ionization parameter is suggestive of CDFS-3865 showing a very hard ionizing spectrum. CDFS-3865 is therefore considered to be young galaxy dominated by massive stars in possibly small regions (expected for young HII regions). Its low metallicity ( $Z \sim 0.1 Z_{\odot}$ ) and large EW(H $\alpha$ ) ( $\sim 800 \text{ \AA}$ ) also support this idea (see also §5.1.2).

Compared to CDFS-3865, most other  $z = 2-3$  galaxies appear to have lower ionization parameters. Notable exceptions are objects found by Fosbury et al. (2003), Erb et al. (2010), and (partly) Richard et al. (2011). Fosbury et al. (2003) and Erb et al. (2010) reveal from their multi-emission lines analysis that their galaxies possess high ionization parameters ( $q_{ion} \gtrsim 10^9 \text{ cm s}^{-1}$ ), low metallicities ( $Z \sim 0.1 Z_{\odot}$  or less), being roughly comparable to (or more or less extreme than) those found in CDFS-3865. Interestingly, both galaxies turn out to exhibit strong Ly $\alpha$  emission. This supports our suggestion that strong Ly $\alpha$  galaxies are in part represented by young galaxies. Richard et al. (2011) also find two lensed galaxies (blue diamonds with upward arrow) possibly have high ionization parameters ( $q_{ion} \gtrsim 10^8 \text{ cm s}^{-1}$ ) judged from their metallicities determined empirically ( $12 + \log(\text{O}/\text{H}) = 8.00^{+0.44}_{-0.50}$  and  $8.77^{+0.14}_{-0.14}$ , for Sextet and MACS0712, respectively). Unfortunately, Ly $\alpha$  measurements are not given in Richard et al. (2011).

However, as indicated by COSMOS-30679, LAEs' ionization parameters are unlikely to be always very high. The ionization parameter for COSMOS-30679 is estimated to be  $q_{ion} = (3.4-15) \times 10^7 \text{ cm s}^{-1}$ , comparable to those found in other high- $z$  galaxies (e.g., Hainline et al. 2009) or LBGs (e.g., Mannucci et al. 2009). Therefore, the ionization parameter is not likely the quantity that distinguishes LAEs from non-LAEs.

Next, we compare our LAEs with galaxies seen in the local universe. According to Dopita et al. (2006), the SDSS galaxies have ionization parameters  $q_{ion} = \text{several} \times 10^7 \text{ cm s}^{-1}$  on average. High- $z$  galaxies including the LAEs appear to have systematically higher ionization parameters than the SDSS galaxies. Galaxies at intermediate redshift ( $z \sim 0.7$ ; Lilly et al. 2003) are also plotted in Figure 7. They show systematically higher [O III]/[O II] ratios than the SDSS galaxies. Since their metallicities are comparable to those of the SDSS galaxies, the offset can be interpreted that higher- $z$  galaxies tend to have higher ionization parameters.

Another interesting comparison is with low-metallicity galaxies in the local universe (gray diamonds). Unlike typical SDSS galaxies, they appear in almost the same parameter space occupied by high- $z$  galaxies on Figure 7. Since their low-metallicities ( $7 \lesssim 12 + \log(\text{O}/\text{H}) \lesssim 8.5$ ) are determined by *direct*  $T_e$  method (e.g., Izotov et al. 2006) and thus reliable, the high [O III]/[O II] ratios can be interpreted as due to high ionization parameters. Indeed, Nagao et al. (2006) suggest that low-metallicity galaxies have higher ionization parameters ( $\gtrsim 3 \times 10^8 \text{ cm s}^{-1}$ ) than more metal-rich galaxies seen in the SDSS sample. Therefore, these low-metallicity galaxies in the local universe appear to have similar metallicities and ionization pa-

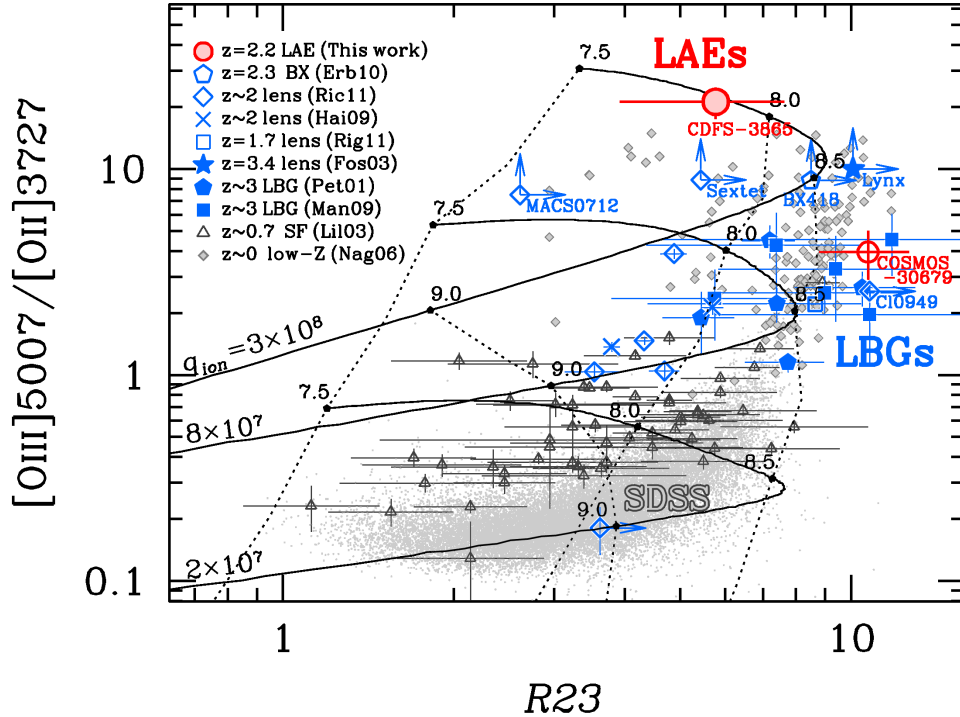


FIG. 7.— The emission line flux ratio  $[O\text{III}]/[O\text{II}]$  vs.  $R23$ -index for our  $z = 2.2$  LAEs (CDFS-3865: the solid red circle, COSMOS-30679: the open red circle) and non-LAEs (the blue symbols); the metal-poor BX galaxy at  $z = 2.3$  (Erb et al. 2010: the open pentagon), lensed galaxies at  $z \sim 2$  (Hainline et al. 2009: the crosses, Richard et al. 2011: the open diamonds, Rigby et al. 2011: the open square), the lensed galaxy at  $z = 3.4$  (Fosbury et al. 2003: the solid star),  $z \sim 3$  LBGs (Pettini et al. 2001: the solid pentagons, Mannucci et al. 2009: the solid squares), as well as the star forming galaxies at  $0.47 < z < 0.92$  (Lilly et al. 2003: the black open triangles), and local star forming galaxies in the low-metallicity range ( $7 \lesssim 12 + \log(O/H) \lesssim 8.5$ : the gray diamonds) and high-metallicity range ( $12 + \log(O/H) \gtrsim 8.2$ : the gray dots) compiled by Nagao et al. (2006). The values on this plot are not corrected for dust extinction, except for the Nagao et al. (2006)’s local data points. The black grid shows photo-ionization model calculations (Kewley & Dopita 2002). For reference, the relations of  $q_{ion} = 3 \times 10^8$ ,  $8 \times 10^7$ , and  $2 \times 10^7 \text{ cm s}^{-1}$  are shown, linked to each other at same metallicities, which are denoted by  $12 + \log(O/H)$  values with dots.

rameters as high- $z$  star-forming galaxies, and particularly those with extreme quantities are likely analogs of high- $z$  LAEs in terms of their high ionization parameters and low metallicities. Among them, star-forming luminous compact galaxies (LCGs), or popularly referred to as “green pea” galaxies (Cardamone et al. 2009) may indeed be good analogs. Although local low-metallicity galaxies tend to have much more modest SFRs than those observed for the LAEs (e.g., Lee et al. 2004), LCGs have comparable SFRs similar to LAEs (Izotov et al. 2011). Based on their low-metallicities (Amorín et al. 2010), strong  $[O\text{III}]$  lines, and distributions in the BPT-diagram (Izotov et al. 2011; see also Fig. 5 of Erb et al. 2010), LCGs are likely to have high ionization parameters ( $\gtrsim 10^8 \text{ cm s}^{-1}$ ). In the SDSS spectroscopic galaxy sample, 139 galaxies are in the low-metallicity range while 48,497 galaxies in the high-metallicity range (Nagao et al. 2006)<sup>18</sup>. Therefore, the local low-metallicity galaxies occupies only  $\sim 0.3\%$  of the SDSS galaxy sample. Similarly, LCGs occupies merely  $\sim 0.07\%$  of the SDSS galaxy sample (Cardamone et al. 2009). Based on the luminosity function determined for the SDSS galaxies (Blanton et al. 2003), the number den-

sity is  $\sim 1.5 \times 10^{-2} \text{ Mpc}^{-3}$  above a detection limit  $M_r = -17.63$ , which corresponds to  $0.037 L^*$ . The limit is calculated from the apparent magnitude limit ( $r < 17.77$ ; Tremonti et al. 2004) for the spectroscopic sample and the redshift threshold ( $z > 0.028$ ; Nagao et al. 2006). The number density of the local low-metallicity galaxies and LCGs are thus approximately  $4.4 \times 10^{-5}$  and  $1.0 \times 10^{-5} \text{ Mpc}^{-3}$ , respectively. On the other hand, the number density of LAEs at  $z = 2.2$  is  $\sim 1.7 \times 10^{-3} \text{ Mpc}^{-3}$  calculated by integrating the luminosity function provided by Hayes et al. (2010)<sup>19</sup> above  $L = 0.037 L^*$ . The number density of the local low-metallicity galaxies is thus more than one order of magnitude smaller than that of LAEs. LCGs seem to be much less abundant by a factor of about four. Such low-metallicity galaxies may be much more abundant at high- $z$  while rarely seen in the local universe.

The final noteworthy implication of the high ionization parameters found in high- $z$  LAEs is that such galaxies may provide additional photons that cause hydrogen reionization of the IGM in the early universe. Previous censuses of early galaxies have revealed a possible shortage of ionizing photons for the cosmic reionization (e.g., Ouchi et al. 2009; Robertson et al. 2010). Ouchi et al. (2009) find that the universe could not be totally ionized by only galaxies at  $z = 7$  if there is no evolution of prop-

<sup>18</sup> Each sample has slightly different conditions such as S/N ratios of lines or redshifts. The direct comparison with the two samples’ numbers is not entirely self-consistent, but provides an approximate ratio.

<sup>19</sup> The detection limit is  $L = 2.8 \times 10^{41} \text{ erg s}^{-1}$  ( $\sim 0.02 L^*$ ).

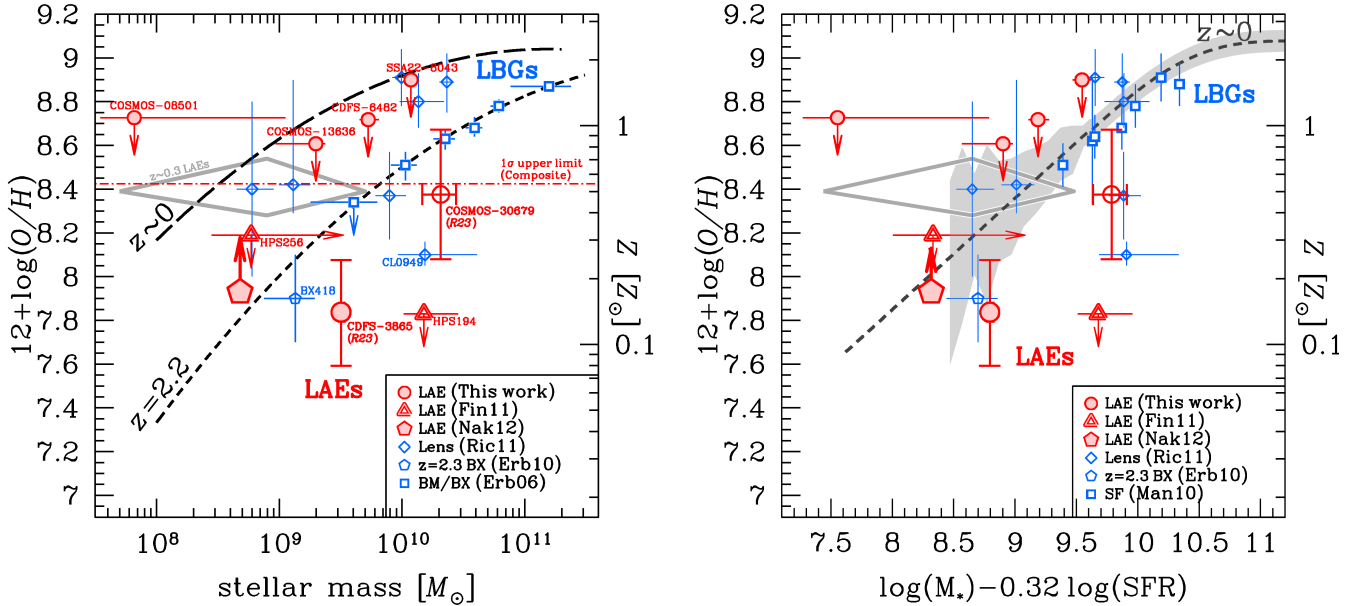


FIG. 8.— (left) Mass-metallicity (M-Z) relation for  $z \sim 2$  LAEs (red symbols), lensed galaxies, and continuum selected galaxies (blue). The circles show our LAEs, whose metallicities are measured/constrained by using  $R23$ -index (with error bar)/ $N2$ -index ( $1\sigma$  upper-limits). The open circle shows COSMOS-30679, whose metallicity range is given with  $2\sigma$ . The red dot-dashed line shows the  $1\sigma$  upper-limit of metallicity ( $N2$ -index) for the composite spectrum in  $K$  band. We additionally plot the average LAE (pentagon: Nakajima et al. 2012) and two  $z \sim 2.4$  LAEs (triangles: Finkelstein et al. 2011). LAEs at  $z = 0.195 - 0.44$  are also shown with gray enclosed area (Cowie et al. 2011). For non-LAEs, we plot lensed galaxies at  $1.5 < z < 2.5$  (open diamonds: Richard et al. 2011), the metal-poor BX galaxy at  $z = 2.3$  (open pentagon: Erb et al. 2010), and BX/BM galaxies (open squares: Erb et al. 2006a). The M-Z relation compiled by Maiolino et al. (2008) at  $z \sim 0$  and  $z \sim 2$  are drawn as long-dashed and dashed curves, respectively. All data plotted here have been recalibrated to have the same metallicity scale (Maiolino et al. 2008) and IMF (Salpeter 1955) except for our LAEs with  $R23$ -index whose metallicities are calibrated with Kewley & Dopita (2002)’s relations. (right) Fundamental metallicity relation proposed by Mannucci et al. (2010). The dashed curve and the shaded areas indicate the relation and its typical dispersions respectively, determined in the local universe (Mannucci et al. 2010, 2011). The open squares show  $z \sim 2$  star forming galaxies collected/compiled by Mannucci et al. (2010) from Erb et al. (2006a) and so on. Other symbols are the same as those in the M-Z relation.

erties (e.g., escape fraction of ionizing photons, metallicity, dust extinction) from  $z \sim 3$  to  $z = 7$ . Since the ionization parameter is by definition a measure of the number of ionizing photons per hydrogen atom, the HII regions are expected to be density-bounded when it is very high. In the conditions of density bounding, more ionizing photons can escape from the HII regions when the ionization parameter is higher (e.g., Brinchmann et al. 2008; Giammanco et al. 2005). Therefore, the escape fraction of ionizing photons is expected to be higher for galaxies (assembly of the HII regions) with higher ionization parameters. Since the fraction of LAEs among star-forming galaxies is known to increase with redshift (e.g., Ouchi et al. 2008; Stark et al. 2010), LAEs and similar low-mass galaxies could produce ionizing photons efficiently and play a key role in supplying ionizing photons for the cosmic reionization at  $z \gtrsim 6$ .

### 5.1.2. Metallicity

Figure 8 (left) shows the observed mass-metallicity (M-Z) relation. The red symbols represent LAEs at  $z \sim 2$ , while the blue symbols show the other galaxies such as LBGs at the similar redshifts. Although some of our LAEs have just weak upper-limits of metallicity due to the lack of  $[\text{N II}]$ -detection (§4.3), for CDFS-3865 and COSMOS-30679, we obtain the metallicity estimates from  $R23$ -index with the oxygen lines. We plot these  $R23$  metallicity estimates with larger circles in Figure 8. Both of them fall below the the conventional M-Z rela-

tion of  $z \sim 2$  LBGs. At least one LAE (HPS194) found by Finkelstein et al. (2011) also looks less chemically-enriched for its mass. Although the offsets of these LAEs from the M-Z relation can be due to the intrinsic scatter of the relation seen in the local universe (e.g., Tremonti et al. 2004), it may also indicate that they are less chemically evolved for their stellar masses. The idea is consistent with the suggestion of their high ionization parameters. Since galaxies with high ionization parameters (e.g., BX418) tend to fall below the M-Z relation as well<sup>20</sup>, young galaxies with high ionization parameters may not follow the M-Z relation defined by more evolved galaxies. Alternatively, differences in star-formation activity may cause the scatter. We discuss this point later.

We also constrain an average metallicity from the  $K$  band composite spectrum (Figure 4) by using the empirical  $[\text{N II}]$ -index. The  $1\sigma$  ( $2\sigma$ ) upper-limit of metallicity is  $12 + \log(\text{O}/\text{H}) < 8.42$  (8.66), which corresponds to  $Z < 0.54$  (0.93)  $Z_{\odot}$ . On the other hand, we independently obtain an average lower-limit of metallicity for LAEs to be  $12 + \log(\text{O}/\text{H}) > 7.93$  (7.63), or  $Z > 0.17$  (0.09)  $Z_{\odot}$  at the  $1\sigma$  ( $2\sigma$ ) level, based on the  $[\text{O II}]/(\text{H}\alpha + [\text{N II}])$  ratio whose fluxes are obtained by stacking 1.18 and 2.09  $\mu\text{m}$  narrowband images for more than 100 LAEs (Nakajima et al. 2012). LAEs thus typi-

<sup>20</sup> Galaxies with high ionization parameter (Fosbury et al. 2003; Richard et al. 2011) are omitted due to their high redshifts ( $z > 2.5$ ). Since the M-Z relation is known to evolve with redshift, a direct comparison with the  $z \sim 2$  LAEs is not appropriate.

cally have a metallicity  $12 + \log(\text{O}/\text{H}) = 7.93\text{--}8.42$  ( $7.63\text{--}8.66$ ) at the  $1\sigma$  ( $2\sigma$ ) level. The range is robust in the sense that the upper-limit is constrained by bright, massive LAEs while the lower-limit by faint, low-mass LAEs. Super-solar metallicities and zero metallicities of Pop III are thus in general unlikely for LAEs in this epoch. The metallicity range also suggests that LAEs at  $z \sim 2$  are rather less chemically enriched than those at  $z \sim 0.3$  ( $12 + \log(\text{O}/\text{H}) \sim 8.4^{21}$ ; Cowie et al. 2011).

Nakajima et al. (2012) find that LAEs fall typically above the M-Z relation below the stellar mass  $\sim 10^9 M_\odot$ . In contrast, the current study finds less chemically enriched LAEs for their masses. This apparent inconsistency may be due to the sampling of a large variety of evolutionary phases within the LAE population. Such variation has been indeed reported by other studies (e.g., Nilsson et al. 2011; Oteo et al. 2012). Alternatively, differences in star-formation activity may cause the inconsistency. To check the possibility, we plot the LAEs on the fundamental metallicity relation (FMR; Mannucci et al. 2010), the relation between stellar mass, metallicity, and SFR. In Figure 8 (right), most of the galaxies at  $z = 0\text{--}2$  including the average LAE (Nakajima et al. 2012) appear to be consistent with the same FMR determined by the SDSS galaxies within their errors. However, some LAEs are significantly below the relation. We can speculate that the FMR is not universal and may fail to reproduce the properties of very young galaxies. Clearly however, much more data is needed to test the idea statistically.

### 5.1.3. Star-Formation Activity

In order to examine the star-formation activity of LAEs, we plot the LAEs on the sSFR versus stellar mass plane in Figure 9. We also plot BX/BM galaxies (Erb et al. 2006b) and sBzK galaxies (Hayashi et al. 2009). We note that this plot should be interpreted with care since the spectroscopic data introduce limits in the sensitivity to low SFRs.

BX/BM and sBzK galaxies follow a simple scaling relation between sSFR and the stellar mass, whose tight relation is referred to as *the star formation main sequence* (e.g., Daddi et al. 2007). Note that BX/BM and sBzK galaxies appear to have slightly different sequences; BX/BMs show lower sSFRs at a given mass. Compared to them, LAEs appear to follow the BX/BMs' main sequence almost over the full mass range. CDFS-3865 and COSMOS-30679, which exhibit high ionization parameters and low metallicities, are not outliers on this diagram. This trend indicates that star-formation activities are well determined by their stellar mass, irrespective of the presence of Ly $\alpha$  emission.

## 5.2. Physical Properties inferred from Ly $\alpha$ and H $\alpha$ emission

### 5.2.1. Correlation between EW(Ly $\alpha$ ) and EW(H $\alpha$ )

Figure 10 shows equivalent widths of Ly $\alpha$  and H $\alpha$  for LAEs (hereafter referred to as the “EWs diagram”). This plot is useful to understand the star-formation histories of LAEs, because the EWs' continuum fluxes evolve in

<sup>21</sup> We recalculate the metallicity by using the Maiolino et al. (2008) indicator. The original estimate is  $\sim 0.15$  dex lower.

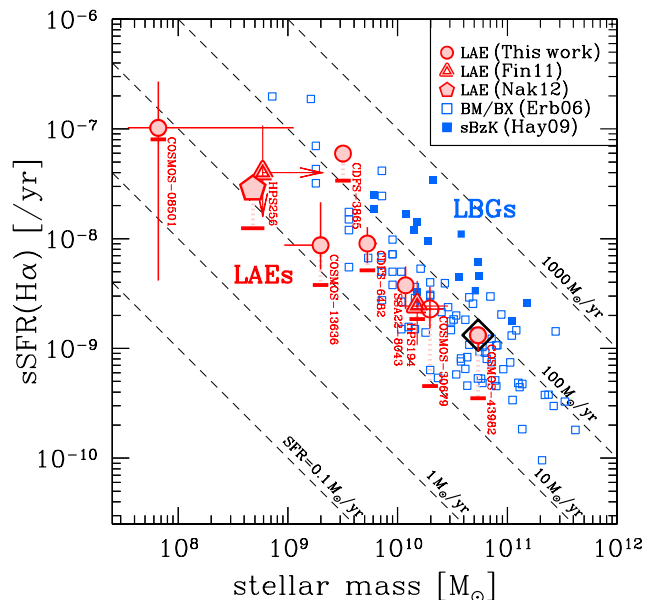


FIG. 9.— Relation between stellar mass and specific star formation rate (sSFR) for  $z \sim 2$  LAEs (red) and continuum selected galaxies (blue); LAEs with NIR spectroscopy (circles: this work, triangles: Finkelstein et al. 2011), the average LAE obtained by stacking NIR NB imaging (pentagon: Nakajima et al. 2012), BX/BM galaxies (open squares: Erb et al. 2006b), and sBzK galaxies (solid squares: Hayashi et al. 2009). COSMOS-43982, a possible object with AGN activity, is marked with black diamond. The red open circle denotes COSMOS-30679, which has less accurate SED fitting results due to the neighbor’s contamination. All sSFRs plotted here are derived from H $\alpha$  luminosity with Salpeter IMF. The short horizontal bars in each symbol for the LAEs indicate the sSFR with no dust extinction correction. The dashed lines correspond to constant SFRs of 0.1, 1.0, 10, 100, and  $1000 M_\odot \text{yr}^{-1}$ .

different ways when different star-formation histories are assumed. Another advantage of using the EWs is that both are pure observables and to zeroth order independent of dust extinction (the effect of dust extinction will be discussed at the end of this section).

The superposed curves on Figure 10 illustrate the evolutions of the EWs for the two extreme star-formation histories, instantaneous burst (dashed) and constant star-formation (solid) at several metallicities (Schaerer 2003)<sup>22</sup>. For the instantaneous burst, since very massive stars ( $M_* \gtrsim 10 M_\odot$ ) complete their evolution within  $\lesssim 10$  Myr, both EWs decline rapidly. As a result, their curves evolve quickly to lower-left on the EWs diagram. For the constant star-formation, on the other hand, the EW(Ly $\alpha$ ) stops declining around  $\sim 100$  Myr, because massive stars that are responsible for both Ly $\alpha$  emission and UV-continuum reach a steady mode. Since the EW(H $\alpha$ ) keeps declining as the older stars build up in the galaxy, their slopes of the evolutionary tracks become less steep on the EWs diagram. Although Schaerer’s calculations stop at  $\sim 400$  Myr for constant star-formation, the EW(Ly $\alpha$ ) varies little after 100 Myr (Charlot & Fall 1993). Therefore, the tracks must extend left almost hor-

<sup>22</sup> The models are collected from the Strasbourg astronomical Data Center (CDS). We present here the three metallicity cases assuming Salpeter IMF (Salpeter 1955) with upper (lower) mass cut-off to be  $100 M_\odot$  ( $1 M_\odot$ ). Case B recombination is assumed for an electron temperature of  $T_e = 3 \times 10^4$  K at zero metallicity and  $T_e = 10^4$  K otherwise, and an electron density of  $n_e = 10^2 \text{cm}^{-3}$ .



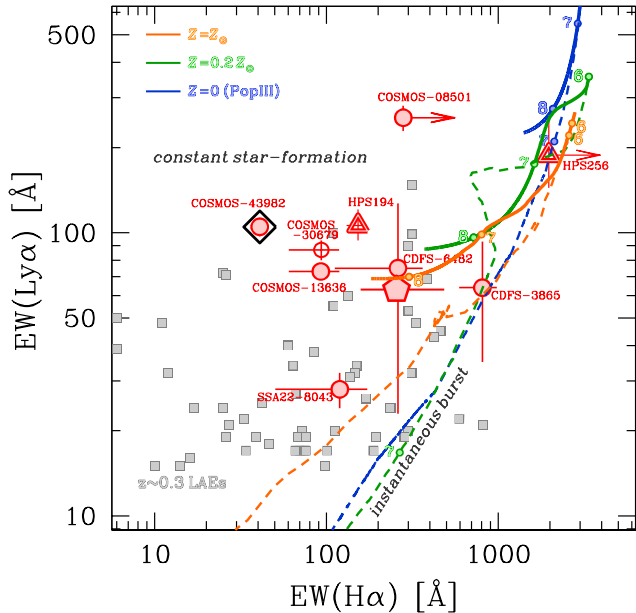


FIG. 10.— Relation between Ly $\alpha$  and H $\alpha$  equivalent widths. The red symbols show  $z \sim 2$  LAEs (same as in Figure 9), and the gray squares show LAEs at  $z = 0.3$  (Cowie et al. 2011). Superposed lines are evolutions of the EWs for instantaneous burst (dashed) and constant star-formation (solid) at metallicities of solar (orange), sub-solar (green), and zero (blue) calculated by Schaerer (2003). Ages are denoted by the numbers (6, 7, 8) near the dots on the lines which indicate (1 Myr, 10 Myr, 100 Myr).

izontally after the terminal points.

Compared with the model predictions, some LAEs with  $\text{EW}(\text{H}\alpha) \sim 1000 \text{ \AA}$ , CDFS-3865, HPS256 (Finkelstein et al. 2011), and possibly COSMOS-08501, can be explained by the instantaneous burst models with very young ages (a few Myr). The other LAEs whose  $\text{EW}(\text{H}\alpha)$  is modest are better described by the constant star-formation models with  $\gtrsim 100$  Myr. Although the sample is small, we find more than half of the LAEs are more consistent with a continuous star-formation history rather than an instantaneous burst. This finding supports our assumption of adopting a constant star-formation history in the SED fitting.

Note, however, that since the EWs are sensitive to recent starbursts, LAEs on instantaneous tracks are not necessarily very young, but can be experiencing a burst after a continuous star-formation. Such a combination of burst plus continuous star-formation is indeed needed to explain the EWs of H $\alpha$  and optical colors observed in local dwarf galaxies (Lee 2006). An LAE with such a combined star-formation history is on a track of instantaneous burst during starburst phases and on a track of constant star-formation for the remaining time. The trend seen in the EWs diagram may be a result that most of the LAEs are not in the burst mode.

Similarly, most of  $z \sim 0.3$  LAEs appear to prefer continuous star-formation on the EWs diagram. Interestingly,  $z \sim 2$  LAEs appear to have systematically higher  $\text{EW}(\text{Ly}\alpha)$  and  $\text{EW}(\text{H}\alpha)$  than lower- $z$  LAEs. Although our spectroscopic sample may be biased toward larger  $\text{EW}(\text{Ly}\alpha)$ , the difference may be a sign that higher- $z$  LAEs are younger. This idea is supported by the inference of lower metallicities at higher- $z$  (§5.1.2).

Although adopting an extended star-formation history

complicates the estimates of metallicity and age from the EWs diagram, independent metallicity estimates would be helpful for constraining its star-formation history and age. E.g., we find CDFS-3865 has a sub-solar metallicity (§4.3). The sub-solar, instantaneous burst track reproduces its EWs well with an age of a few Myr. This very young age is consistent with what we infer for CDFS-3865 from its high ionization parameter and low metallicity (§5.1.1 and §5.1.2). The age roughly agrees with the estimate from the SED fitting. Although some LAEs including COSMOS-30679 have inconsistent age estimates from the EWs diagram and the SED fitting, they can be due to the fact that ages are weakly constrained and luminosity weighted by SED fitting (e.g., Gawiser et al. 2006). Particularly, COSMOS-30679 is thought to have much larger photometric errors (§4.2). Alternatively, their  $\text{EW}(\text{Ly}\alpha)$  may be affected by dust. We discuss the possibility further below. In any case, since age estimates are only possible through SED fitting, the EWs diagram can provide another independent constraint on the stellar populations.

One worry is the effect of dust on Ly $\alpha$ . If the degree of dust extinction is different for Ly $\alpha$  and UV-continuum,  $\text{EW}(\text{Ly}\alpha)$  is no longer independent of dust extinction. In order to examine this effect, we introduce a  $q$  parameter following Finkelstein et al. (2008). The  $q$  parameter is defined as  $q = \tau(\text{Ly}\alpha)/\tau_{1216}$ , where  $\tau(\text{Ly}\alpha)$  and  $\tau_{1216}$  are optical depth for Ly $\alpha$  and UV-continuum at  $\lambda = 1216 \text{ \AA}$ , respectively. Small  $q$  values ( $< 1$ ) mean Ly $\alpha$  photons suffer less attenuation by dust than UV-continuum photons, while large values mean Ly $\alpha$  photons are more heavily attenuated. In the former (latter) case data points go down (up) on the EWs diagram after the corrections. From previous works, LAEs at  $z \sim 2$  have modest  $q$  values; e.g., Hayes et al. (2010) obtain  $q \simeq 1\text{--}1.5$  for  $z = 2.2$  LAEs whose Ly $\alpha$  and H $\alpha$  luminosities are estimated from two narrowbands. Similarly, Nakajima et al. (2012) obtain  $q = 0.7 \pm 0.1$ . Blanc et al. (2011) obtain  $q = 0.99$  for  $z = 2\text{--}4$  LAEs whose intrinsic Ly $\alpha$  luminosities are inferred from UV-continuum. Therefore, assuming  $q = 1$  is reasonable, though we should take care of the possible effect of dust on the EWs diagram.

Another concern involves the validity of the Case B recombination assumption for the LAEs. We discuss the issue in the next section. Along with the discussion so far, however, the EWs diagram shows that LAEs can be well described by the conventional stellar population models and that there is no need to invoke non-standard IMFs.

### 5.2.2. super Case B objects

Figure 11 (left) shows the Ly $\alpha$ /H $\alpha$  ratio against  $\text{EW}(\text{Ly}\alpha)$  for LAEs. The dark red symbols indicate the observed Ly $\alpha$  luminosity divided by the intrinsic H $\alpha$  luminosity corrected using the attenuation inferred from the SED fitting (i.e., showing lower-limits on the  $y$ -axis), while the light red symbols show the observed Ly $\alpha$ /H $\alpha$  ratios. A trend that LAEs with larger  $\text{EW}(\text{Ly}\alpha)$  have larger Ly $\alpha$ /H $\alpha$  ratio appears to be present. This trend itself is not so surprising, but interestingly some LAEs, COSMOS-08501, and possibly COSMOS-13636 and one LAE at  $z \sim 0.3$ , may have Ly $\alpha$ /H $\alpha$  ratios exceeding the Case B recombination value (8.7; Brocklehurst 1971), which we call “super Case B”. Super Case B Ly $\alpha$ /H $\alpha$

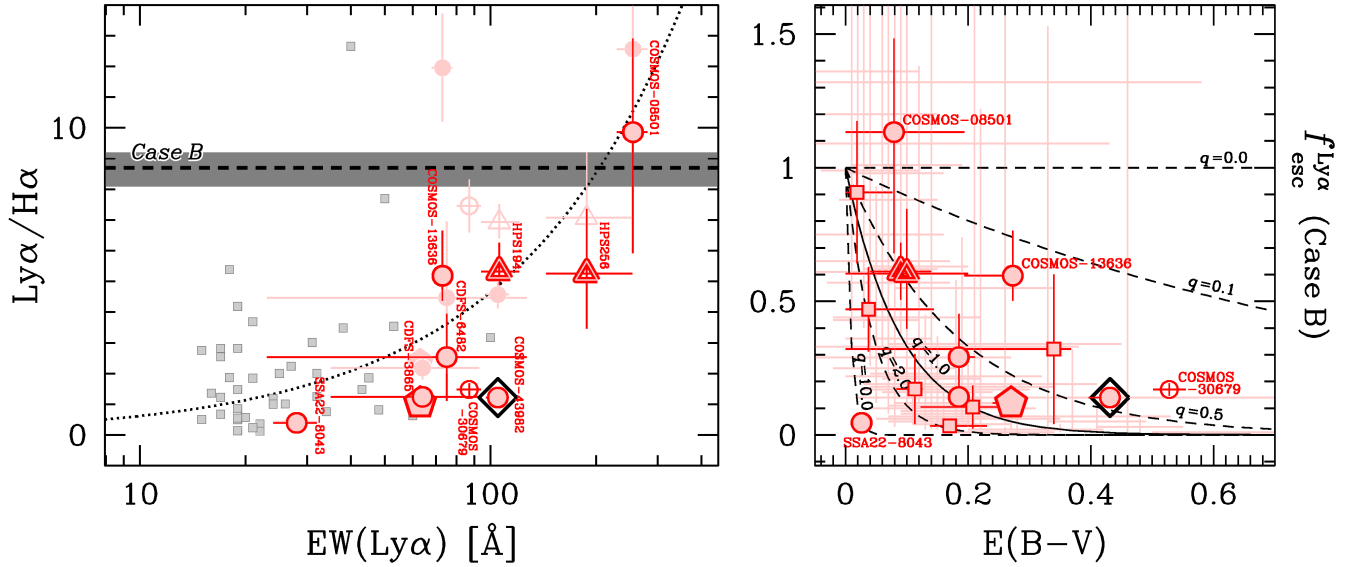


FIG. 11.— (left) Ly $\alpha$ /H $\alpha$  flux ratio vs. EW(Ly $\alpha$ ). Symbols are the same as in Figure 10. The darker symbols show the ratios calculated by the observed Ly $\alpha$  luminosity divided by the intrinsic H $\alpha$  luminosity (i.e., lower-limit of the ratios), while the lighter show the ratios calculated by the observed Ly $\alpha$  and H $\alpha$  luminosities. The ratios for  $z \sim 0.3$  LAEs are based on observed luminosities. Dotted curve represents a single power-law fit given in Eq. (6). The dashed line and the gray shaded area show the Ly $\alpha$ /H $\alpha$  flux ratio assuming the Case B recombination (8.7; Brocklehurst 1971) and its variation with electron density ( $8.1\text{--}9.2$  with  $n_e = 10^2\text{--}10^{10} \text{ cm}^{-3}$ ; Hummer & Storey 1987) when  $T_e = 10^4 \text{ K}$ , respectively. (right) Escape fraction of Ly $\alpha$  photons (assuming the Case B) vs. dust extinction. The red squares show  $z = 2.2$  LAEs (Hayes et al. 2010), and the faint-colored red error bars show  $z = 2\text{--}4$  LAEs (Blanc et al. 2011). Superposed curves show the relations at a given  $q$  parameter ( $q = 0.0, 0.1, 0.5, 1.0, 2.0, 10.0$ ).

ratios have also been reported for some strong LAEs in the local universe (Hayes et al. 2007, Atek et al. 2008, Oti-Floranes et al. 2012, and references therein). The variation of the intrinsic Ly $\alpha$ /H $\alpha$  ratio (the gray shaded area) does not seem to be a significant issue. Although it is not obvious that super Case B objects are included in our sample due to the large errors, we discuss possible physical origins of them in case they really exist.

We consider the possible effect of geometry, and the kinematics of dust and gas in the ISM. Neufeld (1991) propose a clumpy, multi-phase ISM where gas and dust are gathered in clouds within a low-density medium. With such circumstances, Ly $\alpha$  photons can be scattered at the surfaces of the clouds due to the resonant nature, while continuum photons would penetrate the clouds deeply. Since dust is contained in the clouds, Ly $\alpha$  photons would have a much smaller chance of encountering dust than other photons. In this scenario, a large EW(Ly $\alpha$ ) and Ly $\alpha$ /H $\alpha$  ratio can be observed. Alternatively, an outflow of the ISM can be a cause of strong Ly $\alpha$  emission (e.g., Kunth et al. 1998). However, Hashimoto et al. (2012) find an anti-correlation between EW(Ly $\alpha$ ) and Ly $\alpha$  velocity offset for LAEs. Thus, outflows do not appear to be a major mechanism for producing large EW(Ly $\alpha$ ) and Ly $\alpha$ /H $\alpha$  ratio.

In order to clarify the effects of a potentially clumpy geometry of ISM on Ly $\alpha$ /H $\alpha$  ratios, we plot in Figure 11 (right) the relation between  $E(B-V)$  and the escape fraction of Ly $\alpha$  photons ( $f_{\text{esc}}^{\text{Ly}\alpha}$ ) under the Case B recombination assumption. We estimate  $f_{\text{esc}}^{\text{Ly}\alpha}$  as

$$f_{\text{esc}}^{\text{Ly}\alpha} \equiv \frac{L_{\text{obs}}(\text{Ly}\alpha)}{L_{\text{int}}(\text{Ly}\alpha)} = \frac{L_{\text{obs}}(\text{Ly}\alpha)}{8.7L_{\text{int}}(\text{H}\alpha)}, \quad (4)$$

where subscripts ‘int’ and ‘obs’ refer to the intrinsic and observed quantities, respectively. The superposed lines

show the relations at a given  $q$  parameter (§5.2.1);

$$q = \frac{-\log(f_{\text{esc}}^{\text{Ly}\alpha})}{0.4k_{1216}E(B-V)}, \quad (5)$$

where  $k_{1216}$  is an extinction coefficient at  $\lambda = 1216 \text{ \AA}$  (11.98; Calzetti et al. 2000). The clumpy geometry of ISM (or outflow) is favored by objects with  $q = 0\text{--}1$ . From Figure 11 (right), most of the LAEs presented here are located in the range  $q = 0\text{--}1$ ; e.g., COSMOS-30679 and COSMOS-13636 have large  $f_{\text{esc}}^{\text{Ly}\alpha}$  in spite of their moderate amounts of dust. SSA22-8043 has a large  $q$  parameter of  $\sim 10$ , and can be an exception if its Ly $\alpha$  is heavily resonant-scattered by neutral hydrogen gas.

A notable object is COSMOS-08501. It appears to fall above the  $q = 0$  line, where the clumpy ISM model does not work assuming Case B recombination, albeit with relatively large errors. Moreover, since it is inferred to possess relatively small amount of dust, the large EW(Ly $\alpha$ ) owing to the clumpy ISM is unlikely. In case the object is really super Case B, the only remaining explanation is the Ly $\alpha$  enhancement caused by collisional excitations. Due to the decreasing collisional strengths with increasing principle quantum number, collisional excitations can lead to Ly $\alpha$ /H $\alpha$  ratios over the Case B value (see also Osterbrock 1989). Shocks caused by interactions with other sources, AGN activity, supernova explosions, strong outflows or infall are possible candidates for the collisional excitations.

Based on the HST images (Figure 6), COSMOS-08501, a super Case B candidate, looks very compact and shows no sign of interactions. COSMOS-13636, which has a very small  $q$  parameter, shows two faint sources nearby within  $\sim 5 \text{ kpc}$  (projected) from the object. Its strong Ly $\alpha$  emission can be (partly) due to shocks caused by interactions. As discussed by Mori et al. (2004), supernova

explosions can cause strong shocks, resulting in strong Ly $\alpha$  emission. Although the authors intend to explain extended Ly $\alpha$  blobs ( $\sim 100$  kpc) with high Ly $\alpha$  luminosities ( $\sim 10^{43}$  erg s $^{-1}$ ), their basic ideas can be applied to normal LAEs. AGN activity and outflows seem unlikely (see §4.1 and Hashimoto et al. 2012).

When shocks (even partly) contribute to emission lines of LAEs, estimates of physical quantities such as SFR (from H $\alpha$ ), metallicity (from  $N2$ -index), ionization parameter (from [O III]/[O II] ratio), and dust extinction (from Balmer decrement) become less accurate. In particular, the intrinsic H $\alpha$ /H $\beta$  value becomes larger when shocks are present, resulting in an overestimate of the abundance of dust. This effect may also help explain the presence of super Case B objects (e.g., Otí-Flóranes et al. 2012). Thus, the results presented in this paper may require some corrections for the presence of shocks. We plan to address this in future work, through the simultaneous application of photo-ionization and shock models, with deeper spectroscopy which will detect the weaker lines not fully detected in the observations presented here (e.g., Balmer lines, [O II], [O III], [N II], [S II]).

A final remark is that from our discussions so far it is evident that Ly $\alpha$  is not a robust indicator of SFR for LAEs. The observed data ( $z = 0-2$ ) in Figure 11 (left) are relatively well represented by a single power-law fit

$$\log(\text{Ly}\alpha/\text{H}\alpha)_{\text{obs}} = (-1.08 \pm 0.29) + (0.87 \pm 0.19) \times \log \text{EW}(\text{Ly}\alpha), (6)$$

which is shown by the dotted curve in Figure 11 (left). According to this simple relation, SFRs of LAEs with  $\text{EW}(\text{Ly}\alpha) \sim 20 \text{ \AA}$  (a typical threshold in narrowband searches) can be underestimated by a factor of about 10. Thus, SFRs estimated from Ly $\alpha$  may involve a factor of  $\sim 10$  uncertainties intrinsically.

## 6. SUMMARY

We have presented NIRSPEC and MMIRS rest-frame optical spectra of seven Ly $\alpha$  emitters (LAEs) at  $z = 2.2$ , which are selected from our Subaru/Suprime-Cam NB387 survey in COSMOS, Chandra Deep Field South, and SSA22. Our first NIR spectroscopic result discusses the kinematics of LAEs and is presented in Hashimoto et al. (2012). As a companion study, this paper presents mainly the ionization and chemical properties of LAEs based on multiple nebular lines. Our sample includes one possibly AGN-dominated galaxy, and six star-forming galaxies. H $\alpha$  is detected in all six star-forming LAEs, while [N II] $\lambda 6584$  is only detected in the galaxy with signs of AGN activity. Among the six star-forming galaxies, one (CDFS-3865) also has detections of [O II] $\lambda 3727$ , H $\beta$ , and [O III] $\lambda \lambda 5007, 4959$ , and another (COSMOS-30679) has detections of [O II] and [O III]. Our deep  $J$  band spectroscopic observations provide the first [O II]-detections for two individual LAEs at high- $z$ . Our main results are summarized as follows.

- The [O III]/[O II] ratio vs.  $R23$ -index diagram reveals that CDFS-3865 has a very high ionization parameter ( $q_{\text{ion}} = 2.4^{+2.0}_{-0.9} \times 10^8 \text{ cm s}^{-1}$ ) and a low oxygen abundance (metallicity;  $12 + \log(\text{O}/\text{H}) = 7.84^{+0.24}_{-0.25}$ ) in contrast with moderate values of

other high- $z$  galaxies such as LBGs. COSMOS-30679 also has a relatively high ionization parameter ( $q_{\text{ion}} = (3.4-15) \times 10^7 \text{ cm s}^{-1}$ ) and a low metallicity ( $12 + \log(\text{O}/\text{H}) = 8.08-8.67$ ). LAEs would therefore represent an early stage of galaxy formation dominated by massive stars in compact star-forming regions.

- Local low-metallicity galaxies show similar ionization parameters and metallicities to LAEs, and can be local analogs of high- $z$  LAEs. Among them, star-forming luminous compact galaxies (LCGs) may indeed be good analogs, having comparable SFRs similar to LAEs. The local low-metallicity galaxies and LCGs occupies only  $\sim 0.3\%$  and  $0.07\%$  of the SDSS galaxy sample, respectively, and are much rarer by more than one order of magnitude than high- $z$  LAEs.
- Since the escape fraction of ionizing photons is expected to be higher with higher ionization parameters, LAEs and similar low-mass galaxies could produce ionizing photons efficiently and play a key role in supplying ionizing photons for cosmic reionization at  $z \gtrsim 6$ .
- Both CDFS-3865 and COSMOS-30679 fall below the mass-metallicity relation of LBGs at similar redshifts. Their low metallicities do not seem to be explained by their star formation rates being taken into account, albeit with their relatively large error. Interestingly, galaxies with high ionization parameters tend to fall below the relation. Very young galaxies may not follow the relation determined by more evolved galaxies.
- The composite spectrum independently provides an upper-limit on the metallicity of  $12 + \log(\text{O}/\text{H}) < 8.42$  ( $< 8.66$ ) at the  $1\sigma$  ( $2\sigma$ ) level. Combined with a lower-limit of metallicity (Nakajima et al. 2012), LAEs typically have metallicities  $12 + \log(\text{O}/\text{H}) = 7.93-8.42$  ( $7.63-8.66$ ) at the  $1\sigma$  ( $2\sigma$ ) level.
- In contrast to the large differences in ionization parameters and metallicity between LAEs and LBGs, we find LAEs have similar specific star formation rates as BX/BM galaxies at a given stellar mass.
- We show that the  $\text{EW}(\text{Ly}\alpha)$  vs.  $\text{EW}(\text{H}\alpha)$  diagram is useful for understanding the star-formation histories of LAEs, being relatively independent of SED fitting. According to the EWs diagram, more than half of the LAEs appear to need an extended star-formation such as a burst superimposed upon a continuous star-formation (exponentially declining or constant) rather than the instantaneous burst alone.
- LAEs with low  $q$ -values ( $q = 0-1$ ) can be explained by the clumpy geometry of ISM. Interestingly, our sample may include objects with further enhanced Ly $\alpha$ , which we call super Case B. If they really exist, the only possible explanation is the collisional excitations of Ly $\alpha$ . Interactions with other sources and/or supernova explosions are possible

key events that may cause shock-induced collisional excitation. If such shocks play a role in enhancement of the Ly $\alpha$  flux, physical quantities such as SFR, metallicity, ionization parameter, and dust extinction should be re-computed using a combination of photo-ionization and shock-excitation models. We plan to investigate the role of shocks further in future works.

We are grateful to the staff of the W. M. Keck Observatory and Subaru telescope who keep the instruments and telescopes running effectively. Without their generous support, most of the observations presented here would

not have been possible. We also thank T. Yoshikawa and M. Hayashi for their assistance with NIR spectroscopy data reduction, T. Nagao and R. Maiolino for providing the data of emission lines for local galaxies, and T. Hayashino for providing the imaging data in the SSA22 field. The NewH $\alpha$  Survey team is thanked for providing their *J* band image of SSA22. This work was supported by World Premier International Research Center Initiative (WPI Initiative), MEXT, Japan, and KAKENHI (23244025) Grant-in-Aid for Scientific Research (A) through Japan Society for the Promotion of Science (JSPS). KN acknowledges support from the JSPS through JSPS research fellowships for Young Scientists.

*Facilities:* Keck II (NIRSPEC), Magellan:Clay (MMIRS), Subaru (Suprime-Cam)

## REFERENCES

- Allende Prieto, C., Lambert, D. L., & Asplund, M. 2001, *ApJ*, 556, L63
- Amorín, R. O., Pérez-Montero, E., & Vílchez, J. M. 2010, *ApJ*, 715, L128
- Atek, H., Kunth, D., Hayes, M., Östlin, G., & Mas-Hesse, L. M. 2008, *A&A*, 488, 491
- Baldwin, J. A., Phillips, M. M., & Terlevich, R. 1981, *PASP*, 93, 5
- Bertin, E., & Arnouts, S. 1996, *A&AS*, 117, 393
- Blanc, G. A., et al. 2011, *ApJ*, 736, 31
- Blanton, M. R., et al. 2003, *ApJ*, 592, 819
- Bond, N. A., Gawiser, E., Gronwall, C., Ciardullo, R., Altmann, M., & Schawinski, K. 2009, *ApJ*, 705, 639
- Brinchmann, J., Pettini, M., & Charlot, S. 2008, *MNRAS*, 385, 769
- Brocklehurst, M. 1971, *MNRAS*, 153, 471
- Bruzual, G., & Charlot, S. 2003, *MNRAS*, 344, 1000
- Capak, P., et al. 2004, *AJ*, 127, 180
- Cardamone, C., et al. 2009, *MNRAS*, 399, 1199
- Calzetti, D., Armus, L., Bohlin, R. C., Kinney, A. L., Koornneef, J., & Storchi-Bergmann, T. 2000, *ApJ*, 533, 682
- Charlot, S., & Fall, S. M. 1993, *ApJ*, 415, 580
- Cowie, L. L., & Hu, E. M. 1998, *AJ*, 115, 1319
- Cowie, L. L., Barger, A. J., & Hu, E. M. 2011, *ApJ*, 738, 136
- Daddi, E., et al. 2007, *ApJ*, 670, 156
- Dopita, M. A., et al. 2006, *ApJ*, 647, 244
- Erb, D. K., Shapley, A. E., Pettini, M., Steidel, C. C., Reddy, N. A., & Adelberger, K. L. 2006a, *ApJ*, 644, 813
- Erb, D. K., Steidel, C. C., Shapley, A. E., Pettini, M., Reddy, N. A., & Adelberger, K. L. 2006b, *ApJ*, 647, 128
- Erb, D. K., Pettini, M., Shapley, A. E., Steidel, C. C., Law, D. R., & Reddy, N. A. 2010, *ApJ*, 719, 1168
- Finkelstein, S. L., Rhoads, J. E., Malhotra, S., Grogan, N., & Wang, J. 2008, *ApJ*, 678, 655
- Finkelstein, S. L., et al. 2011, *ApJ*, 729, 140
- Förster Schreiber, N. M., et al. 2009, *ApJ*, 706, 1364
- Fosbury, R. A. E., et al. 2003, *ApJ*, 506, 797
- Furusawa, H., et al. 2008, *ApJS*, 176, 1
- Gawiser, E., et al. 2006, *ApJ*, 642, L13
- Gawiser, E., et al. 2007, *ApJ*, 671, 278
- Giacconi, R., Rosati, P., Tozzi, P., et al. 2001, *ApJ*, 551, 624
- Giammanco, C., Beckman, J. E., & Cedrés, B. 2005, *A&A*, 438, 599
- Gray, R. O., & Corbally, C. J. 1994, *AJ*, 107, 742
- Gronwall, C., et al. 2007, *ApJ*, 667, 79
- Guaita, L., et al. 2010, *ApJ*, 714, 255
- Guaita, L., et al. 2011, *ApJ*, 733, 114
- Hainline, K. N., Sharpley, A. E., Kornei, K. A., Pettini, M., Buckley-Geer, E., Allam, S. S., & Tucker, D. L. 2009, *ApJ*, 701, 52
- Hashimoto, T., et al. 2012, arXiv:1206.2316
- Hayashi, M., et al. 2009, *ApJ*, 691, 140
- Hayashino, T., et al. 2004, *AJ*, 128, 2073
- Hayes, M., et al. 2007, *MNRAS*, 382, 1465
- Hayes, M., et al. 2010, *Nature*, 464, 562
- Hummer, D. G., & Storey, P. J. 1987, *MNRAS*, 224, 801
- Izotov, Y. I., Stasińska, G., Meynet, G., Guseva, N. G., & Thuan, T. X. 2006, *A&A*, 448, 955
- Izotov, Y. I., Guseva, N. G., & Thuan, T. X. 2011, *ApJ*, 728, 161
- Kauffmann, G., et al. 2003, *MNRAS*, 346, 1055
- Kennicutt, R. C., Jr. 1998, *ARA&A*, 36, 189
- Kewley, L. J., Dopita, M. A., Sutherland, R. S., Heisler, C. A., & Trevena, J. 2001, *ApJ*, 556, 121
- Kewley, L. J., & Dopita, M. A. 2002, *ApJS*, 142, 35
- Kunth, D., Mas-Hesse, J. M., Terlevich, E., Terlevich, R., Lequeux, J., & Fall, S. M. 1998, *A&A*, 334, 11
- Kurucz, R. 1993, Kurucz CD-ROM 13 (Cambridge, MA: SAO)
- Lee, J. C., Salzer, J. J., & Melbourne, J. 2004, *ApJ*, 616, 752
- Lee, J. C. 2006, PhD thesis, Univ. Arizona
- Lee, J. C., et al. 2012, arXiv:1205.0017
- Lilly, S. J., Carollo, C. M., & Stockton, A. N. 2003, *ApJ*, 597, 730
- Ly, C., et al. 2011, *ApJ*, 726, 109
- Ly, C., Malkan, M. A., Kashikawa, N., Ota, K., Shimasaku, K., Iya, M., & Currie, T. 2012, *ApJ*, 747, L16
- Madau, P. 1995, *ApJ*, 441, 18
- Maiolino, R., et al. 2008, *A&A*, 488, 463
- Malhotra, S., & Rhoads, J. E. 2002, *ApJ*, 565, 71
- Mannucci, F., et al. 2009, *MNRAS*, 398, 1915
- Mannucci, F., Cresci, G., Maiolino, R., Marconi, A., & Gnerucci, A. 2010, *MNRAS*, 408, 2115
- Mannucci, F., Salvaterra, R., & Campisi, M. A. 2011, *MNRAS*, 414, 1263
- McLinden, E. M., et al. 2011, *ApJ*, 730, 136
- Miyazaki, S., et al. 2002, *PASJ*, 54, 833
- Mori, M., Umemura, M., & Ferrara, A. 2004, *ApJ*, 613, L97
- Nagao, T., Maiolino, R., & Marconi, A. 2006, *A&A*, 459, 85
- Nakajima, K., et al. 2012, *ApJ*, 745, 12
- Neufeld, D. A. 1991, *ApJ*, 370, L85
- Nilsson, K. K., et al. 2009, *A&A*, 498, 13
- Nilsson, K. K., Östlin, G., Möller, P., Möller-Nilsson, O., Tapken, C., Freudling, W., & Fynbo, J. P. U. 2011, *A&A*, 529, 9
- Oke, J. B. 1974, *ApJS*, 27, 21
- Ono, Y., Ouchi, M., Shimasaku, K., Dunlop, J., Farrah, D., McLure, R., & Okamura, S. 2010, *ApJ*, 724, 1524
- Osterbrock, D. E. 1989, *Astrophysics of Gaseous Nebulae and Active Galactic Nuclei*. University Science Books, Suva, CA
- Oteo, I., et al. 2012, arXiv:1202.0997
- Otí-Flóranes, H., et al. 2012, arXiv:1207.7303
- Ouchi, M., et al. 2003, *ApJ*, 582, 60
- Ouchi, M., et al. 2008, *ApJS*, 176, 301
- Ouchi, M., et al. 2009, *ApJS*, 706, 1136
- Overzier, R. A., et al. 2008, *ApJ*, 673, 143
- Pagel, B. E. J., Edmunds, M. G., Blackwell, D. E., Chun, M. S., & Smith, G. 1979, *MNRAS*, 189, 95
- Peng, C. Y., Ho, L. C., Impy, C. D., & Rix, H. 2010, *AJ*, 139, 2097
- Pettini, M., et al. 2001, *ApJ*, 554, 981
- Pirzkal, N., Malhotra, S., Rhoads, J. E., & Xu, C. 2007, *ApJ*, 667, 49
- Richard, J., Jones, T., Ellis, R., Stark, D. P., Livermore, R., & Swinbank, M. 2011, *MNRAS*, 413, 643

- Rigby, J. R., Wuyts, E., Gladders, M. D., Sharon, K., & Becker, G. D. 2011, *ApJ*, 732, 59
- Roussetot, P., Lidman, C., Cuby, J. G., Moreels, G., & Monnet, G. 2000, *A&A*, 354, 1134
- Robertson, B. E., Ellis, R. S., Dunlop, J. S., McLure, R. J., & Stark, D. P. 2010, *Nature*, 468, 49
- Salpeter, E. E. 1955, *ApJ*, 121, 161
- Schaerer, D. 2003, *A&A*, 397, 527
- Schaerer, D. & de Barros, S. 2009, *A&A*, 502, 423
- Scoville, N., et al. 2007, *ApJS*, 172, 1
- Shimasaku, K., et al. 2006, *PASJ*, 58, 313
- Stark, D. P., Ellis, R. S., Chio, K., Ouchi, M., & Bunker, A. 2010, *MNRAS*, 408, 1628
- Steidel, C. C., Adelberger, K. L., Kurt L., Shapley, A. E., Pettini, M., Dickinson, M. & Giavalisco, M. 2000, *ApJ*, 532, 170
- Tremonti, C. A., Heckman, T. M., Kauffmann, G., et al. 2004, *ApJ*, 613, 898
- van Dokkum, P. G. 2001, *PASP*, 113, 1420
- Venemans, B. P., et al. 2005, *A&A*, 431, 793
- Yan, H., et al. 2005, *ApJ*, 634, 109
- York, D. G., et al. 2000, *AJ*, 120, 1579
- Yoshikawa, T., et al. 2010, *ApJ*, 718, 112